Assessment of the properties to characterize the interface between clay brick substrate and strengthening mortar

João A.P.P. Almeida[a,*], Davide Bordigoni[b]; Eduardo N. Pereira[a], Joaquim A.O. Barros[a], Alessandra Aprile[b]

[a]ISISE, Dep. of Civil Eng, University of Minho, Azurém, 4810-058 Guimarães, Portugal

[b]Dep. of Eng., University of Ferrara, 44121 Ferrara, Italy

* Corresponding author.

E-mail addresses: japp.almeida@gmail.com (J.A.P.P. Almeida); davide.bordigoni@student.unife.it (D. Bordigoni); epereira@civil.uminho.pt (E.N. Pereira); barros@civil.uminho.pt (J.A.O. Barros); alessandra.aprile@unife.it (A. Aprile)

HIGHLIGHTS

- The interface properties between PFRM strengthening overlay and the ceramic brick substrate was analysed.
- The mechanical characterisation of the interface based on direct shear tests was developed and discussed.
- The failure modes obtained experimentally were used to assess the orthotropic mechanical properties of the interface.
- The constitutive laws of the interface considering Mohr and Mohr-Coloumb failure criteria were assessed based on the direct shear test results.

ABSTRACT

The behaviour of masonry elements under in-plane and out-of-plane loads can be improved through the application of strengthening systems based on reinforcing overlays. After strengthening, the transition region between the original substrate and

the strengthening layer is especially stressed, and premature failure of the strengthened masonry is reached if insufficient interfacial capacity is assured. Therefore, the assessment of the mechanical behaviour of the interface is critical to the development of the masonry strengthening system based on the application of strengthening overlays.

In this research a method for the characterization of the interface behaviour between two different materials, a polypropylene fibre reinforced mortar (PFRM) and a ceramic brick used for masonry construction is presented. Direct shear tests were carried out in couplet specimens. Due to the orthotropic nature of the bricks surface, the shear load was applied along three different directions in order to perform an overall estimation of the interface behaviour. The peak and residual shear stresses, as well as the failure modes, were obtained at different levels of the normal stress. Based on these experimental results constitutive laws were assessed for the simulation of the interface mechanical behaviour based on the Mohr and Mohr-Coulomb failure criteria.

Keywords: Interface behaviour; Shear response; Direct shear test; Failure criteria; Masonry strengthening overlay.

Nomenclature:

FRCM	fabric reinforced cementitious matrix
PFRM	polypropylene fibre reinforced mortar used in the FRCM system
A_e	effective interface area between the two units
c	cohesion
$c^*_{0,p}$	initial apparent cohesion
c^*_p	peak apparent cohesion
$\emptyset_{0,p}$	initial friction angle
$\emptyset_p$	friction angle
μ	tangent of friction angle
N	vertical load
τ	shear stress
τ_p	peak tangential stress
τ_r	residual tangential stress
$\tau_{c,i}$	tangential values estimated by the criterion
$\tau_{e,i}$	tangential experimental values
$\bar{\tau}_e$	tangential mean value of the experimental results
T_p	peak horizontal load
T_r	residual horizontal load
σ	normal stress
χ	tensile strength
χ'	residual tensile strength

1. INTRODUCTION

Masonry was one of the main techniques used in the construction of old structures and still is widely used in new buildings. Nevertheless, it is in the case of already existing buildings that masonry often plays a key role as a structural component. The evolution of the design codes has tended to impose more demanding requirements, especially in the case of the action in seismic regions. Consequently, due to this and other durability driven performance insufficiencies, techniques to retrofit existing masonry constructions have recently been developed, and their performance evaluated. These techniques aim to fulfil higher demands in terms of load bearing capacity and increase the ductility response of masonry elements.

A considerable number of strengthening techniques are nowadays based on the application of reinforcing overlays. These systems often show vulnerability at the level of the interface due to the sharp gradient of mechanical properties between the substrate and the reinforcing material [1]. This work presents an experimental program developed with the aim of characterizing the mechanical properties of the interface between a polypropylene fibre reinforced mortar (PFRM) strengthening overlay, which is part of a FRCM based masonry strengthening system, and a masonry substrate. The results obtained were used to derive the orthotropic constitutive laws of the interface based on both the hyperbolic Mohr and the Mohr-Coloumb failure criteria.

1.1. Overlay strengthening techniques

Additional strengthening overlays can be applied to existing masonry with the aim of improving its structural behaviour. This technique is of special importance in areas of high seismic activity, as a means to comply with the current code requirements in terms of resistance to horizontal loading, in particular the seismic action. Typically, the strengthening overlay can be applied manually or mechanically, and is composed by a cement mortar matrix and a reinforcing mesh. The tensile and ductility behaviour of the strengthening overlay is improved by using fibres and meshes made of steel, polymers,

carbon or glass [2-8]. The application of these reinforced strengthening overlays improves both the in-plane and the out-of-plane load carrying capacity of the masonry [9]. Alternatively, the overlay strengthening system can be composed of materials showing tensile strain-hardening behaviour in the hardened state, avoiding the use of reinforcement meshes. These materials, typically designated as strain hardening cementitious composites (SHCC), reach tensile strengths higher than the stress at crack initiation, and ultimate tensile strains clearly exceeding 1%. These materials typically develop diffuse crack patterns while loaded in tension, and the maximum crack width remains controlled typically below a maximum of 0.1 mm in the hardening phase. SHCC materials can be applied using the shotcreting technique or manually [10-11]. SHCC based strengthening systems can lead to the increase of the shear capacity of the masonry, to the improvement of its deformability and to the enhancement of its energy dissipation capacity during cyclic loading [12].

Some of the advantages and disadvantages of the masonry strengthening techniques that are based on the addition of strengthening overlays to the original masonry element are presented by Elgaway et al. [2], [13]. The advantages identified include the low cost, the durability, the uniform behaviour, the increase of in-plane strength up to 3.6 times, the improvement of the out-of-plane stability, and the increase of the energy dissipation ability before failure. The increase of the dead weight of the strengthened elements, the requirement of surface treatments, the architectural changes of the structure, and the high disturbance during works are the main disadvantages identified [2], [13].

1.2. Experimental characterization of the interface behaviour

1.2.1. Test setups

The mechanical response of the interface between different materials subjected to shear loads is an important topic both in the design of new construction and in the rehabilitation of existing structures [14-16]. In particular, regarding the interface properties of masonry substrates, several authors have conducted research on the assessment of the shear

force-slip response of the interface between units [17-21]. The testing schemes used to perform the experiments are diverse, mainly regarding the specimen's geometry, boundary conditions and loading configurations adopted during testing. Some of the most popular loading arrangements and specimen geometries are presented by Van Der Pluijm [22] and Montazerolghaem et al. [23]. Although distinct loading arrangements have been tried, introducing a pure shear stress distribution in a joint is nearly impossible, as well as to achieve a totally uniform shear and normal stress distribution along the interface [22].

The characterization of the shear behaviour of mortar joints according to the standard EN1052-3 [24] is carried out by performing the triplet tests. However, according to Hofmann et al. [25] and Montazerolghaem et al. [23], this test setup induces local stress concentrations, as shown in Figure 1. The approximated normal and the shear stresses were obtained using linear finite element analysis. These stress concentrations directly disturb the evenness of stress distribution in both ends of the mortar joint. The failure modes show a clear trend for the occurrence of stepped crack, which can introduce unwelcomed rotations, as reported by Lourenço et al. [26].

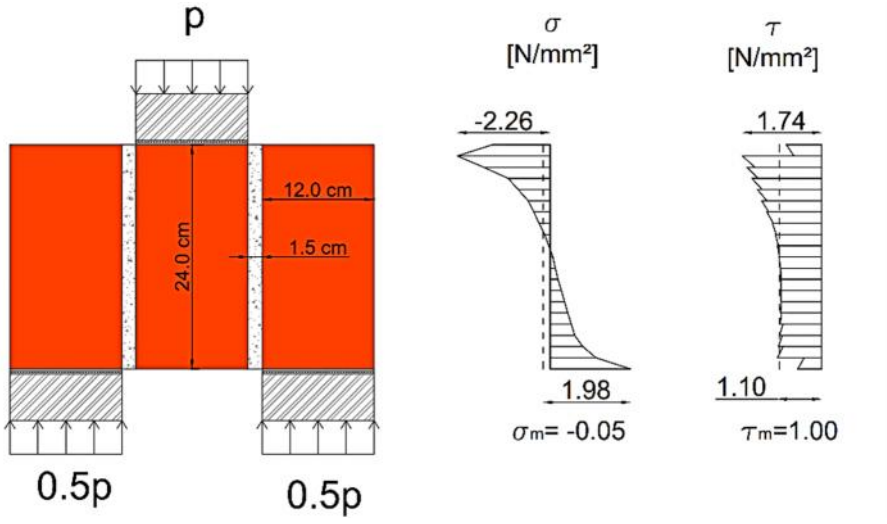

Figure 1 - Triplet test Shubert arrangement, adapted from [25].

The numerical evaluation performed by Hofmann et al. [25] shows that the couplet setup of Hofmann, presented in Figure 2, leads to a better approximation of a uniform shear

stress distribution along the joint than other test setups. Nevertheless, the test setup is too complex to adopt as standard method. A simplified version of this test setup is presented by DIN, see Figure 3, leading to an almost uniform shear stress, even if an appreciable uneven normal stress distribution occurs at the joint.

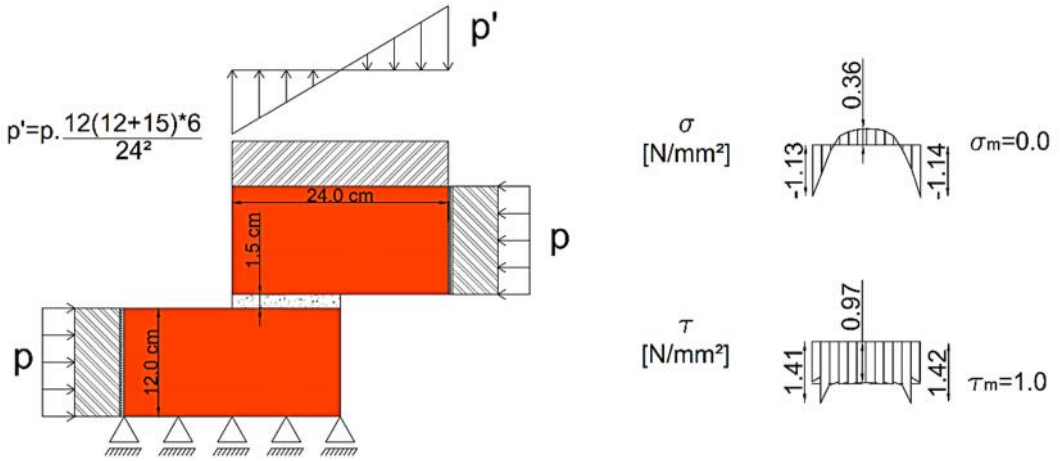

Figure 2 - Couplet test Hofmann arrangement, adapted from [25].

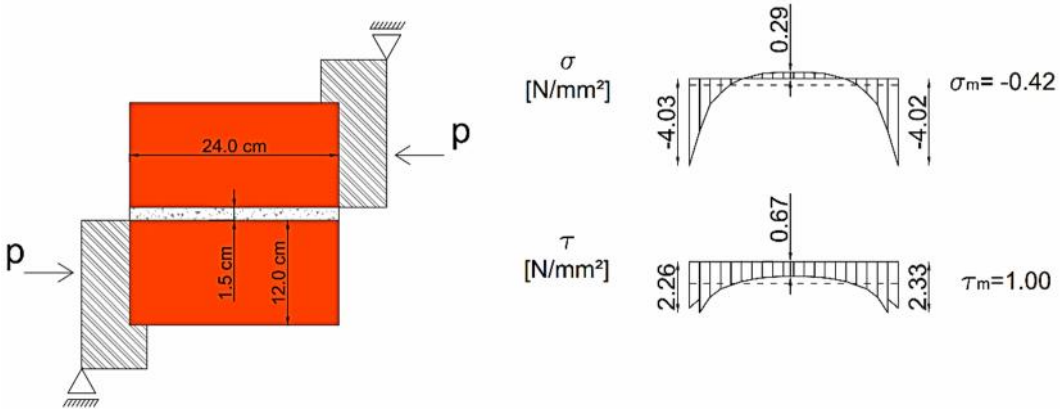

Figure 3 - Couplet test DIN arrangement, adapted from [25].

An alternative shear test setup proposed by Vasconcelos and Lourenço [18] also uses a specimen with two units, see Figure 4. In this case the specimen is placed between two thick steel plates and attached to the steel plates by steel bolts, so that the shear force can be transmitted to the specimen. Thin steel sheets are attached to the steel plates to concentrate the shear load as close as possible to the bed joint, aiming to prevent bending moments and to provide a more uniform shear stress distribution. In addition,

two thin sheets of Teflon are placed between the steel plates and the specimens to minimize bending effects due to friction.

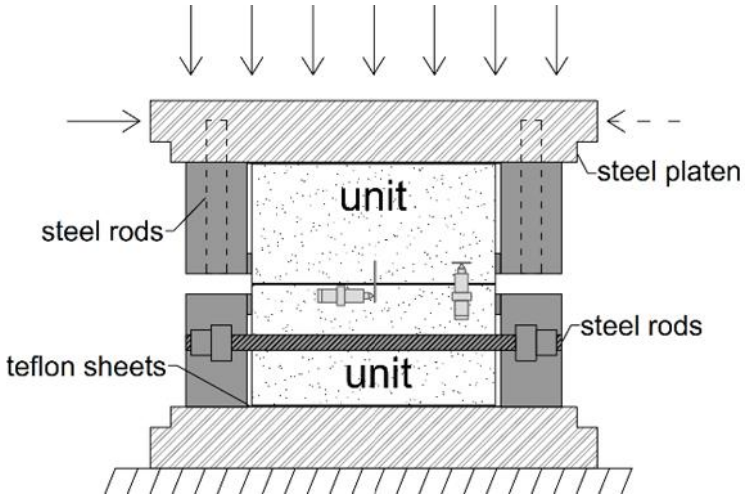

Figure 4 - Test setup used to perform cyclic direct shear tests, adapted from [18].

1.2.2. Data derived from the tests

The values of the two strength parameters, cohesion c or f_{v0} as described by EN1052-3 [24], and the tangent of the friction angle $\mu = \tan\varphi$, for different types of interfaces obtained by triplet and couplet tests are presented in Table 1.

Table 1 - Strength parameters for different types of interfaces.

Source	Type of test	Interface	c (f_{v0}) (N/mm^2)	μ
Lourenço et al. [26]	Triplet	Concrete brick /Micro-concrete	1.39	1.03
Gabor et a. [27]	Triplet	Ceramic brick/Cement mortar	1.60	0.90
Alecci et al. [19]	Triplet	Ceramic brick/Cement mortar	0.53	--
Vasconcelos and Lourenço [28]	Couplet	Granite/Lime mortar	0.36	0.63
Abdou et al. [20]	Couplet	Ceramic brick/Cement mortar	1.61	1.05

1.3. Mohr and Mohr Coulomb failure criteria

The shear strength and shear force-slip response at the interface between the masonry substrate and the strengthening overlay is not unique, but dependent on the level of normal stress applied. In general, the material strength under a multiaxial stress state may be considered as a function of that stress state, and cannot be determined exclusively by either the tensile, the compressive or the shearing stresses independently of each other. A considerable number of failure criteria has been proposed, [29],

assuming this consideration. The most commonly used in the case of isotropic materials is the Mohr criterion, which states that failure is governed by the following relation, see equation (1):

$$|\tau| = f(\sigma) \quad (1)$$

where the local shear strength, τ, considering a specific plane, is dependent only on the normal stress, σ, at the same plane.

The equation (1) represents the failure envelope of the corresponding Mohr circles considering all possible stress states. The envelope $f(\sigma)$ can assume different shapes and can be determined experimentally. Considering the case of a hyperbolic shape, the simplest case is described by the equation (2) [30]:

$$f(\sigma) = \pm\sqrt{(c - \sigma \times \tan\emptyset)^2 - (c + \chi \times \tan\emptyset)^2} \quad (2)$$

where χ is the tensile strength, c the cohesion and $\emptyset$ the friction angle.

According to the Mohr's criterion, the material failure will occur at all states of stress for which the largest of Mohr's circles is tangent to the envelope.

An alternative and simpler shape of the Mohr envelope was proposed by Coulomb and is characterized by one straight line, as shown in Figure 5, and represented by equation (3) [31].

$$f(\sigma) = c - \sigma \times \tan\emptyset \quad (3)$$

The Mohr-Coulomb criterion is often preferred to describe the experimental results of mechanical tests on interfaces [20], [26], [28]. On the other hand, the use of Mohr hyperbolic criterion is not so common due to its additional complexity. Examples of its use on numerical modelling can be found in [32] and [33].

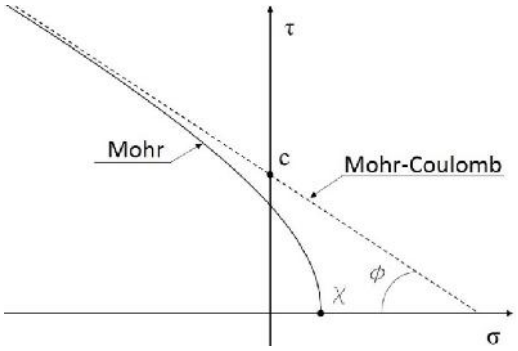

Figure 5 – Schematics of Mohr-Coulomb and Mohr failure criteria for positive tangential stresses.

2. OBJECTIVES AND RESEARCH SIGNIFICANCE

The determination of the mechanical properties of the interface between masonry substrates and PFRM strengthening overlays is regarded as essential for the optimisation of the performance of the FRCM strengthening system considered, since the interface is typically one of the weakest links in the system. Therefore, this research is dedicated to experimentally characterise the mechanical response of the interface between the masonry substrate and the strengthening overlay by performing direct shear tests. Therefore, this research is dedicated to the experimental characterisation of the mechanical response of the interface between the masonry substrate and the strengthening overlay by performing direct shear tests. In addition, the applicability of the analytical Mohr and the Mohr-Coloumb loading/failure criteria to approximate or predict the experimental results are discussed. These results may constitute an important step for the development of a constitutive model that represents the interface behaviour for general states of stress or deformation.

3. MATERIALS AND METHODS

3.1. Characterization of materials

The mechanical properties of the materials used to assemble the specimens tested in direct shear were characterized. The ceramic bricks were tested in compression, while PFRM specimens in the hardened state were tested in compression and flexure. The

PFRM specimens were casted from the same mixtures used to produce the specimens for the direct shear tests. This procedure allowed to determine the properties of all mixtures used in the direct shear tests, since the curing conditions and the compositions were kept the same.

3.1.1. Characterization of ceramic brick

The type of ceramic brick selected, with 8 hollow cells, is regionally common, and is represented in Figure 6. The dimensions are 30×20×11 cm^3, respectively the length, width and thickness. The compressive strength of the ceramic brick was obtained by following the experimental procedure proposed by EN 772-1 [34]. The tests were carried out under load control, with the loading direction at perpendicular and parallel relatively to the holes longitudinal axis, with the application of a load rate of 1.10 and 1.65 kN/s, respectively. The average compressive strength and coefficient of variation obtained for 6 specimens in both cases were 2.21 (9 %) MPa, and 6.55 (8%) MPa, where the value in round brackets is the coefficient of variation.

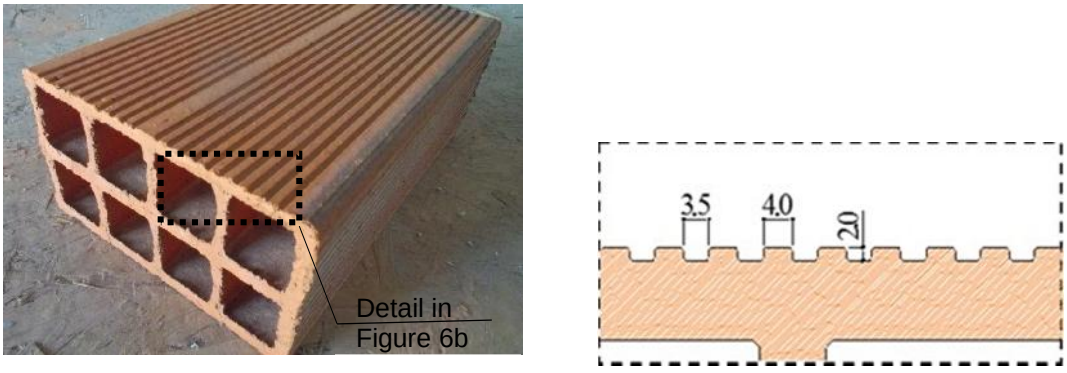

a) b)

Figure 6 – Ceramic brick used to mount the specimens: a) ceramic brick; b) detail of grooves, dimensions in mm.

3.1.2. Characterization of the PFRM in the hardened state

To characterize the evolution of the mechanical properties of the PFRM in the hardened state, three different curing ages were considered, 28, 56 and 84 days. For each curing age 12 specimens were tested in bending and 24 were tested in compression. All

mixtures of PFRM were prepared using the same amount of water. The weight ratio of *water/dry material* was set to 0.14, considering that the dry material includes the binder, polymer fibres, aggregates and additives, as provided by the manufacturer of the pre-packed mixture.

Specimens with dimensions of 160x40x40 mm^3 were tested in bending by adopting the procedure described in EN 1015-11 [35] for three point bending tests (TPB). The tests were carried out under displacement control by applying a constant displacement rate at mid-span equal to 2.5 μm/s. The compressive tests of the PFRM followed the procedure proposed by EN 1015-11 [35] according to which from each tested TPB specimen two specimens with dimensions of 40x40x70 mm^2 were obtained. The 24 specimens were tested under load control, by imposing a loading rate equal to 0.4 kN/s. The maximum load obtained was registered to calculate the compressive strength.

The mean values of the compressive strength and of the equivalent tensile strength in flexure, f_c and f_{ft}, as well as the corresponding coefficients of variation, are presented in Table 2 for the different curing ages. The evolutions of the minimum, maximum and average values of the compressive strength and the equivalent tensile strength in flexure with respect to the curing age are shown in Figure 7. The average tensile strength in flexure exceeded 6 MPa before 28 days, whereas the average compressive strength exceeded 40 MPa slightly before the 56 days. After 28 days of curing these properties seem do not alter significantly.

Table 2 – Summary of experimental results.

Curing age	Flexural Tensile Strength		Compressive Strength	
	f_t	CoV	f_c	CoV
(days)	(MPa)	(%)	(MPa)	(%)
28	6.59	6.5	38.22	16.1
56	6.93	10.8	41.49	11.1
84	6.95	8.6	41.87	4.8

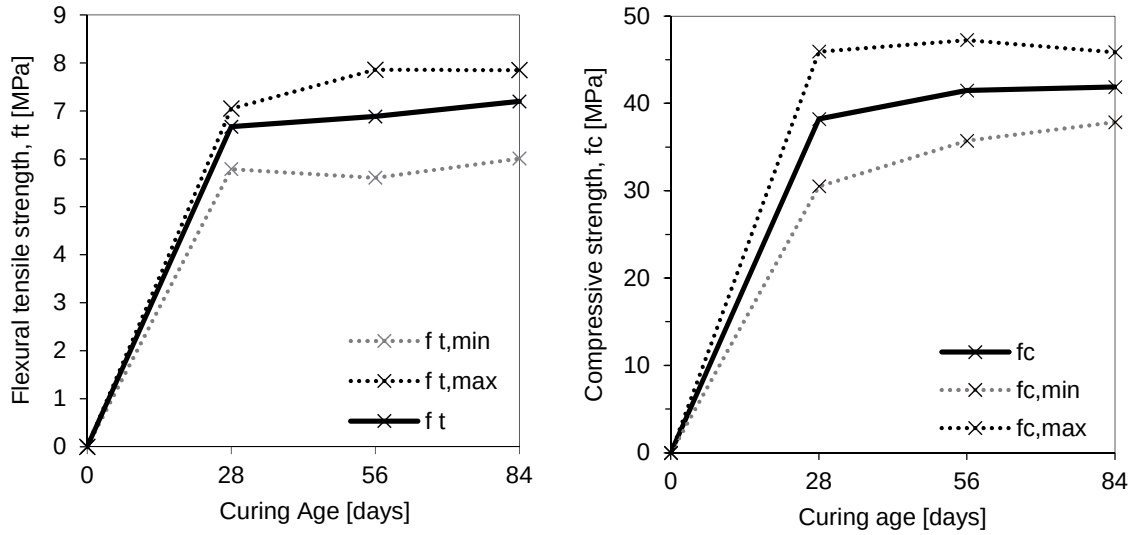

a) b)

Figure 7 - Evolution of the hardened state properties of the PFRM: a) equivalent tensile strength in flexure vs curing age; b) compressive strength vs curing age.

3.1.3. Pull-off of mortar patch from ceramic brick

The adhesion strength between the mortar and the ceramic brick was assessed by means of pull-off tests according the standard EN 1015-12, [36]. The specimens with 30x20x13.5 cm^3 were produced and cured at constant temperature and relative humidity of approximately 20ºC and 90%, respectively. The preparation of the samples for testing started with the execution of a circular slot with 50 mm diameter, using a core drilling machine. After cleaning the surface, a metallic plate was bonded to the test area using an epoxy resin. The metallic plate was later attached to the pull-off machine, a Proceq-Z15, which has a maximum traction force of 16 kN, a free course of 3.5 mm and an accuracy greater than 98 %. The test procedure consisted on applying a traction force to the mortar surface through the circular plate. After the initial levelling of the equipment, the increasing traction force was applied at a constant loading rate of 40 N/s. The maximum force recorded corresponds to the adhesion force. The pull-off tests were carried out at 28 days after casting. The adhesive strength between the mortar and the ceramic brick was estimated using the contact area of each specimen, see Figure 8.

Based on the results of 16 tested specimens, an average adhesion strength of 0.6 MPa and a coefficient of variation equal to 14% were obtained.

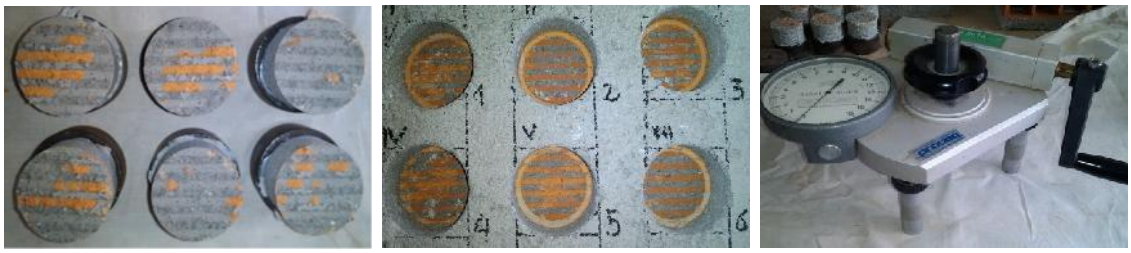

a) b) c)

Figure 8 - Pull-off test: a) detached PFRM layer; b) surface of the bricks after testing; c) pull-off device.

3.2. Preparation of the specimens for the direct shear tests

In order to consider the orthotropic characteristics of the brick surface, with a pattern composed of grooves in one direction, three shear loading orientations were investigated for assessing the interface shear behaviour and its relation to the loading direction with respect to the brick surface pattern (0º, 45º and 90º, see Figure 9).

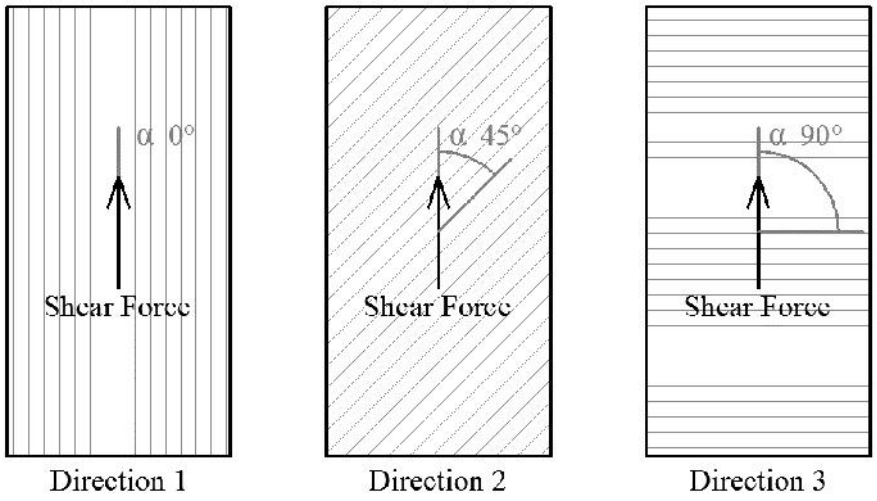

Figure 9 - Representation of the loading directions investigated.

In Table 3 the labels of all specimens for each batch of PFRM are shown, as well as the curing age when tested. The number of specimens tested for each of the three loading directions, 0º, 45º and 90º, was defined considering the need to identify the most appropriate failure criterion to describe the observed experimental responses.

Table 3 - Summary of the samples tested for each mortar batch.

Mix	Curing age	Samples
1	56 days	A1, A2, A4, B1, B3, D4
2	56 days	E1, E4, F1, F2, F3, F4, G2, G3, G4, H2, H3, I1, L1, L2, L3, L4, M1, M2, P1, P2, P3
3	28 days	N1, N2, Q1, Q2, R1, R2, R3, S2

The initiation and propagation of the shear crack along the interface plane was assured by means of two notches executed along the longer faces of the specimens. In this fashion, the effective contact area between the two units was decreased to 60% of the initial area at this localization region. The sequence of steps carried out for the preparation of the specimens is detailed in Figure 10 and described subsequently:

- cutting of the bricks in two parts to obtain the surface for testing (Figure 10.a);
- casting of the mould containing the brick part with the PFRM in order to create a compact and regular unit with a height of 80 mm (Figure 10.b);
- removing of the framework after one week and turning the unit upside down (Figure 10.c);
- pouring the PFRM fresh mortar on top of the existing unit (Figure 10.d);
- cutting the specimens to obtain four or three specimens from each prism depending on the testing direction (Figure 10.e);
- execution of two notches in both lateral longitudinal faces to impose the formation of the failure surface along the interface between the two materials;
- measurement of the effective dimensions of the specimens and labelling (Figure 10.f).

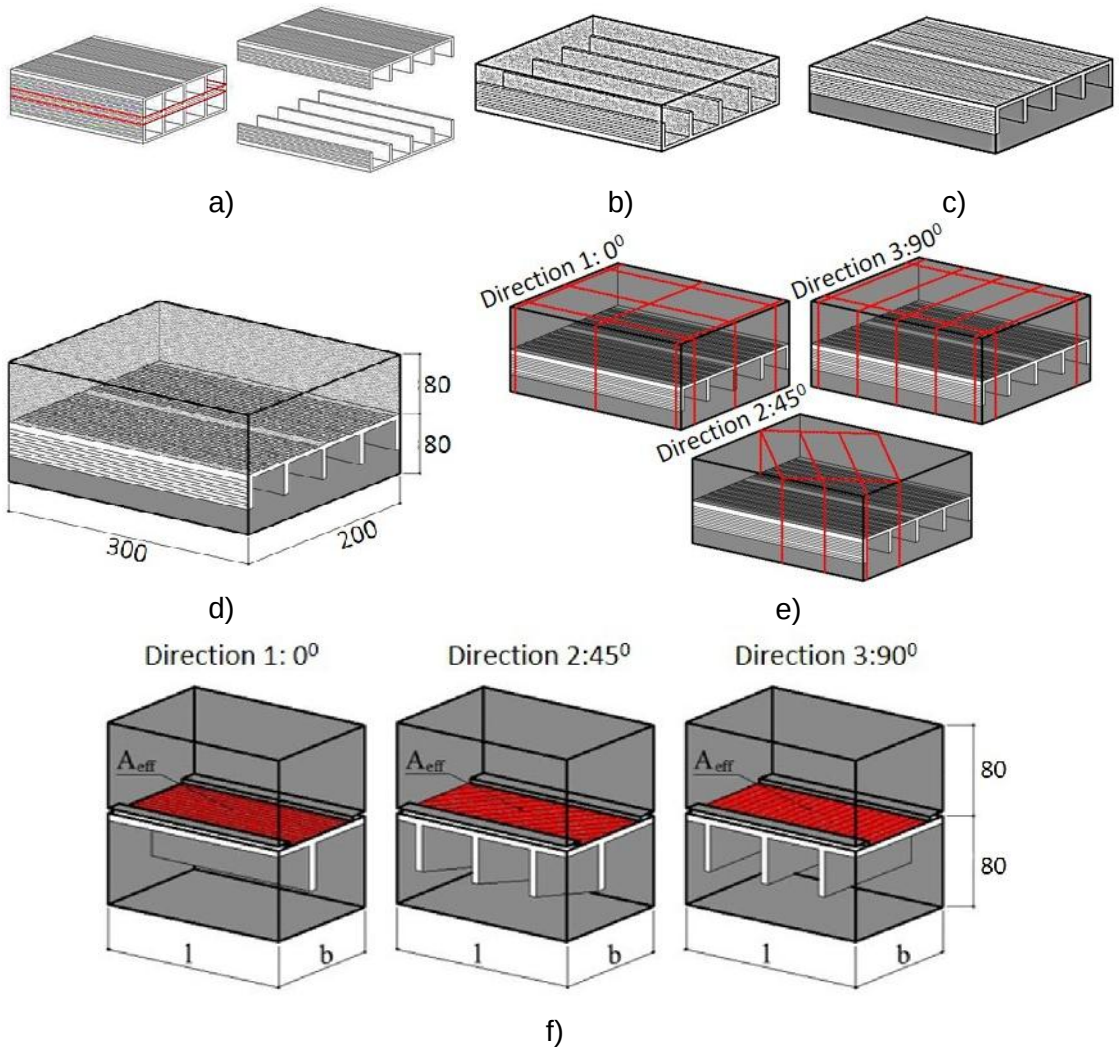

Figure 10 – Preparation of specimens: a) cutting the bricks; b) pouring mortar to create a compact and regular unit; c) demolding and turning the unit upside down d) brick samples after casting; e) detailing of the cutting lines for obtaining the final specimens; f) final preparations on the specimens, including the execution of the lateral notches. Dimensions in mm.

3.3. Test setup and procedures

The stiffness of the reaction frame was checked before starting the tests. Shear tests are typically brittle, therefore the reaction frame must be stiff enough to allow the capturing of the softening part of the shear response in a controlled manner. Thus, one cycle of loading, up to 32 kN, and unloading was applied directly on the reaction system, since in preliminary tests was verified that the samples have reached peak shear forces in the interval 10 to 25 kN. The elastic response of the reaction frame revealed a maximum

displacement, measured by two transducers and averaged, equal to 55 μm at a maximum load of 32 kN, corresponding to a constant stiffness of K=590 kN/mm.

The test setup is shown in Figure 11 and Figure 14, where the A-unit represents the part of the specimen composed of the PFRM exclusively, whereas the B-unit represents the part of the specimen that contains the brick element. The horizontal displacement of the B-unit was constrained by means of a rigid support on the opposite side of the actuator in order to impose a relative sliding between the two units.

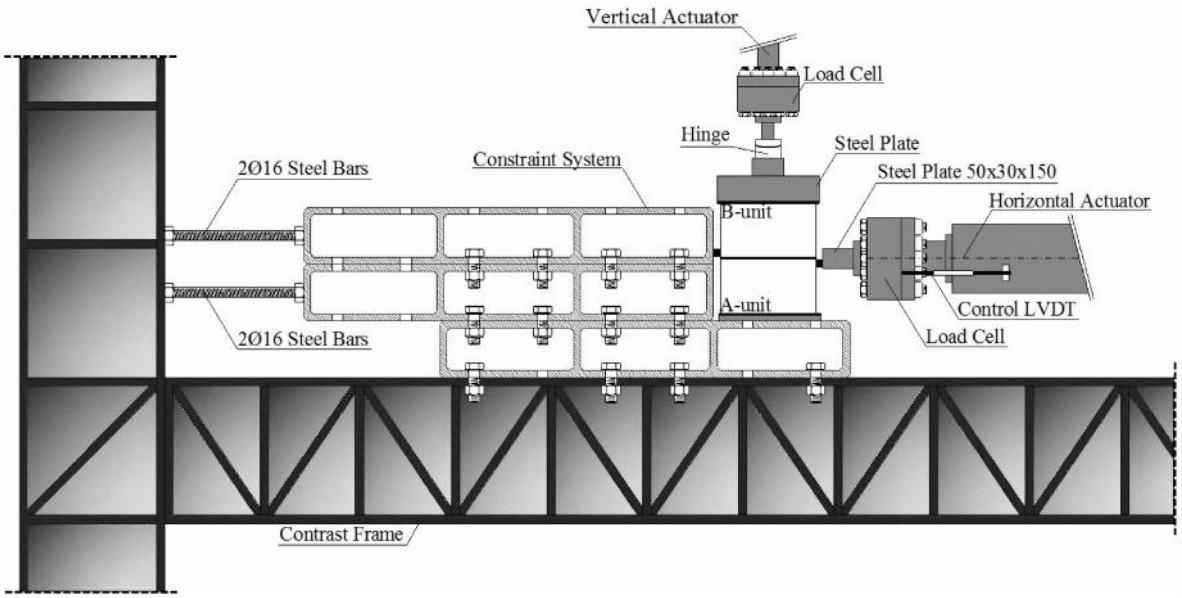

Figure 11 - Test setup global view.

To minimize the vertical distance between the load applied in the horizontal direction and the reciprocal reaction, and therefore minimize the moment causing the rotation of the specimen, a steel bar with the dimensions of 10x10x150 mm^3 was placed at the loaded surface of each unit, between the specimen and the actuator crosshead, and between the specimen and the reaction frame as well, see Figure 12. By minimizing the distance between the imposed force and corresponding reaction, also the bending moment at the interface, which is responsible for modifying the normal stress distribution, was minimized. Furthermore, two layers of thin aluminium plates, with a Teflon sheet in-

between, were placed on the top and on the bottom of the specimen in order to minimize the tangential stresses on the external surfaces (Figure 12).

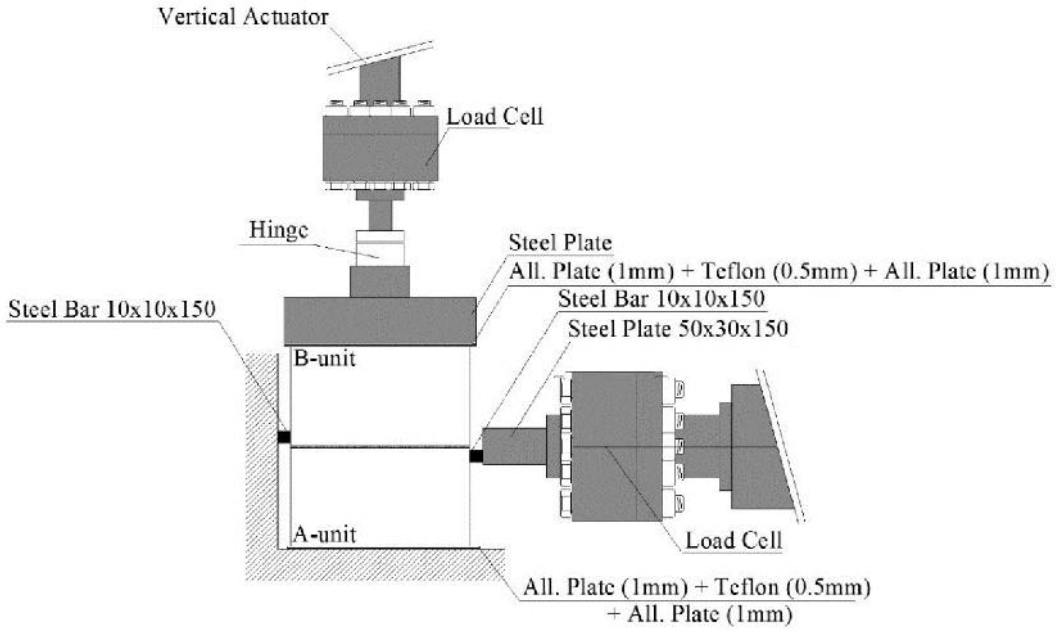

Figure 12 – Detail of the setup developed for the direct shear test.

The testing procedure adopted consisted on imposing a controlled displacement in the horizontal direction at a constant load in the vertical direction. The horizontal displacement rate was 0.001 mm/s until reaching 0.6 mm, and subsequently 0.002 mm/s until the end of the test. The vertical actuator was used to apply the constant vertical load by means of a hinge and a rigid steel plate to distribute evenly the load on the top surface of the specimen.

Four linear variable displacement transducers (LVDT) were installed on both unloaded faces of the specimen (front and rear faces of the specimen) for monitoring the relative vertical displacement and the sliding between the two units. The transducers were positioned on the opposite corners of the samples, as shown in Figure 13.

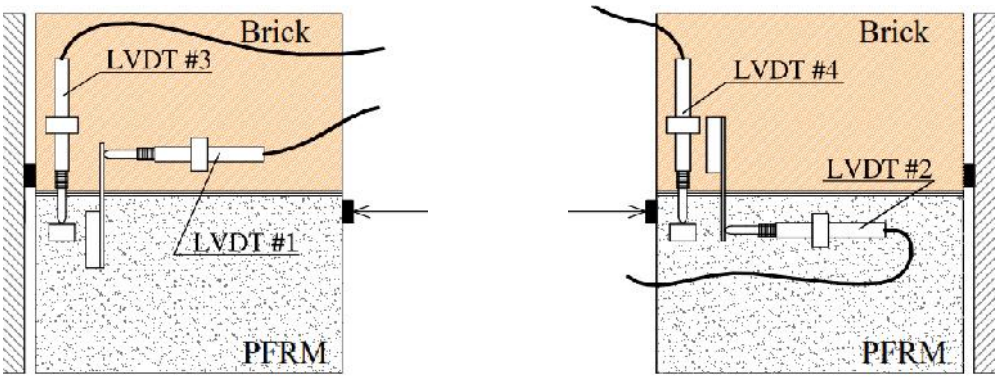

a) b)

Figure 13 – Position of LVDTs in the specimen: a) Front face, position of LVDT#1 and LVDT#3; b) Rear face, position of LVDT#2 and LVDT#4.

a) b)

Figure 14 – Setup of the direct shear test: a) general view; b) detail of the specimen during testing.

4. DIRECT SHEAR TEST RESULTS

4.1. Peak and residual shear stresses

The evaluation of the overall results was carried out in terms of the average values. The vertical stress, σ, the peak tangential stress, τ_p, and the residual tangential stress, τ_r, were calculated by means of the equations (4) to (6), respectively:

$$\sigma = \frac{N}{A_e} \quad (4) \qquad \tau_p = \frac{T_p}{A_e} \quad (5) \qquad \tau_r = \frac{T_r}{A_e} \quad (6)$$

where T_p and T_r are, respectively, the peak and the residual horizontal load measured by the load cell, N is the vertical load and A_e is the effective area of contact between the two units.

The residual values of the tangential stress were considered equal to the tangential stress obtained when the slope of the tangential stress-slip response reached a minimum common value among all the specimens tested, as described subsequently. The experimental responses in terms of the tangential stress, τ, versus the slip, s, were linearized considering the slope for a constant slip increment equal to 0.01 mm, see equation (7). In order to exclude the effect of the local scatter of the experimental results, the average slope, $\overline{K}t_{0.3m}$, was evaluated by computing the central moving average for a slip of 0.3 mm considering $n = 30$, see equation (8). The maximum slope $\overline{K}t_{0.3m}$ observed simultaneously in all the responses, -0.331 MPa/mm, was considered as the reference threshold for the evaluation of the residual tangential stress, τ_r.

$$\mathrm{Kt} = \frac{\Delta\tau}{0.01\ m} \qquad (7) \qquad\qquad \overline{K}t_{0.3m} = \frac{\sum_{i-1}^{n} K_i}{n} \qquad (8)$$

The results obtained for the different directions tested, 0°, 45º and 90º orientation, are shown in Table 4, where the PFRM mixtures used to cast the samples and the effective area, A_e , are also indicated.

Table 4 - Experimental results.

Direction	Mix	Specimen	A_{eff} (mm^2)	σ (MPa)	τ_p (MPa)	τ_r (MPa)
1	1	A1	7342	0.23	3.35	0.48
		A2	5054	0.38	3.55	0.63
		A4	4847	0.45	3.89	0.73
		B1	6926	0.22	3.38	0.43
		B3	4992	0.46	4.16	0.78
		D4	5123	0.35	3.47	0.86
	2	E1	6028	0.36	3.82	1.04
		E4	5719	0.99	4.27	-
		F1	5764	2.04	5.52	3.13
		F2	4420	1.44	5.29	2.29
		F3	5940	1.50	5.19	2.17
		F4	5852	1.50	4.68	2.24
2	3	N1	5109	0.35	2.86	0.75
		N2	5016	0.26	2.94	0.40
	2	P1	4454	1.53	4.61	2.03
		P2	5412	0.15	2.50	0.80
		P3	4454	0.35	2.76	0.85
	3	Q1	4620	2.00	4.85	2.49
		Q2	4323	1.00	3.97	1.89
		R1	5320	0.35	3.05	0.80
		R2	5148	1.51	4.15	2.07
		R3	5280	0.25	2.74	1.01
		S2	4978	0.16	2.57	0.74
3	2	G2	5254	1.57	4.10	2.28
		G3	5720	0.35	2.76	1.06
		G4	5325	0.30	2.81	0.64
		H2	6580	0.97	3.69	1.89
		H3	5040	0.26	2.60	0.65
		I1	6248	0.25	2.47	0.85
		L1	4935	0.15	2.49	0.33
		L2	5076	0.16	2.39	-
		L3	4970	2.00	4.38	2.74
		L4	5396	1.50	4.40	2.66
		M1	4512	0.15	2.55	0.33
		M2	4230	0.36	2.91	0.41

In Figure 15, Figure 16 and Figure 17 the tangential stress *versus* the average slip responses are shown for each level of the imposed vertical stress. The average slip was obtained by averaging the two horizontal transducers installed at the two opposite unloaded faces of the specimens. The results obtained are divided into two groups, depending on the imposed normal stress during testing. The lower imposed normal stress results group include responses obtained for values below 0.5 MPa.

The $\tau - s$ responses obtained are essentially composed by three stages. The pre-peak stage is characterized by a linear rapid increase of the tangential stress for very low slip values, while the interface remains intact, and by a short non-linear branch immediately

before the peak shear stress is reached. The second stage is composed by a post-peak branch that is characterized by a non-linear decrease of the load for an increasing value of the slip. The third stage is composed by the final softening branch that corresponds to a progressive reduction of the cohesion before the reaching of an approximately constant frictional resistance.

The results obtained showed that for higher normal stress the slip at peak increased and the overall response was more ductile. The dispersion of results obtained for direction 2 (45º) was lower than the one registered for direction 1 (0º).

The $\tau - s$ responses obtained for direction 3 (90º), see Figure 17, reveal several local peaks in the softening branch. These results are explained by the fact that, for the 90° orientation series, the crack propagation along the interface was more progressive due to a sequential rupture of the brick ribs. A dispersion of results intermediate of the two previsous cases (0º and 45º) was obtained for the 90º series.

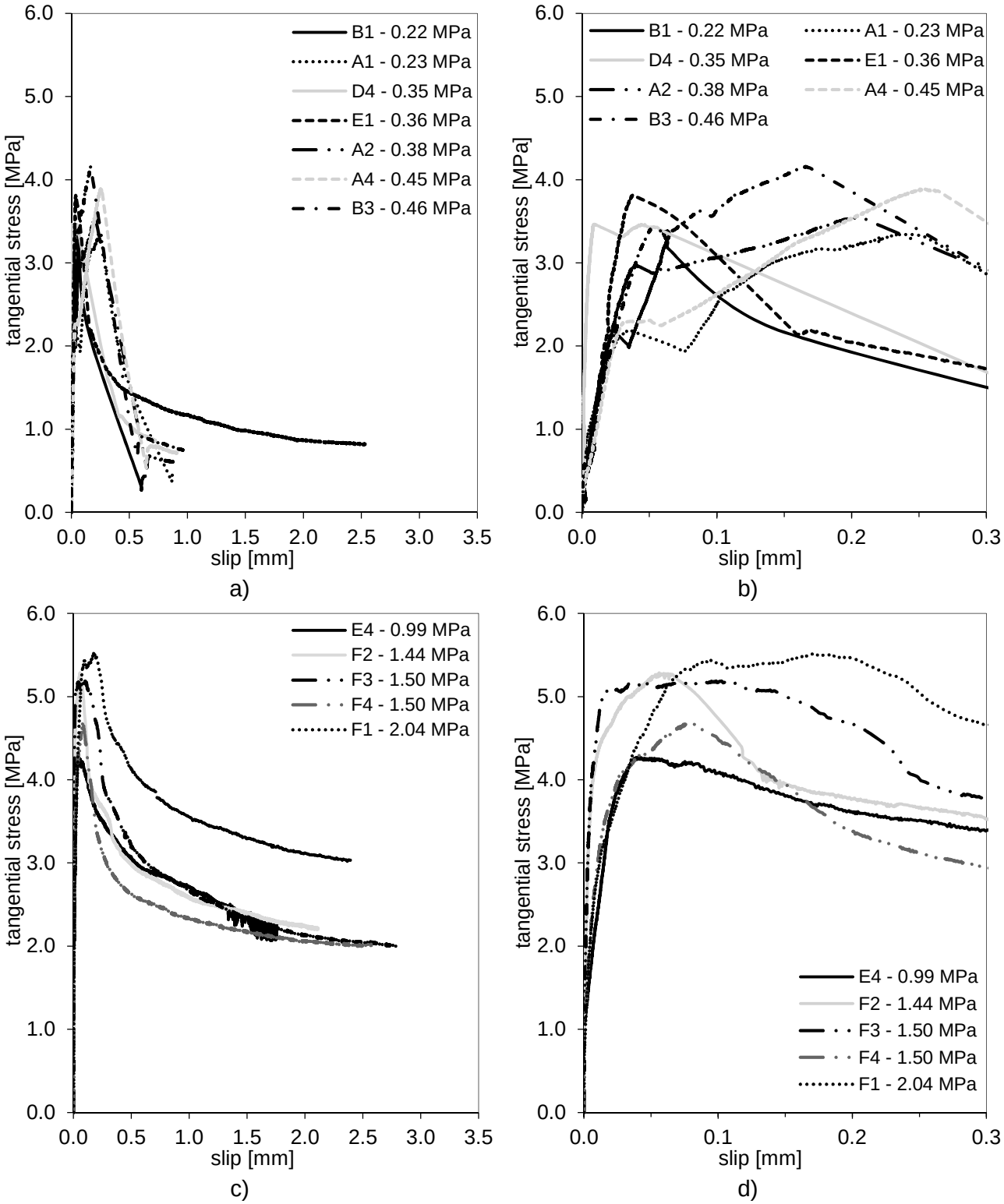

1 Figure 15 - τ-s responses for direction 1 (0º): a) and b) responses for lower imposed normal
2 stresses; c) and d) responses for higher imposed normal stresses; b) and d) detail of the initial
3 stage up to an average slip of 0.3mm.
4

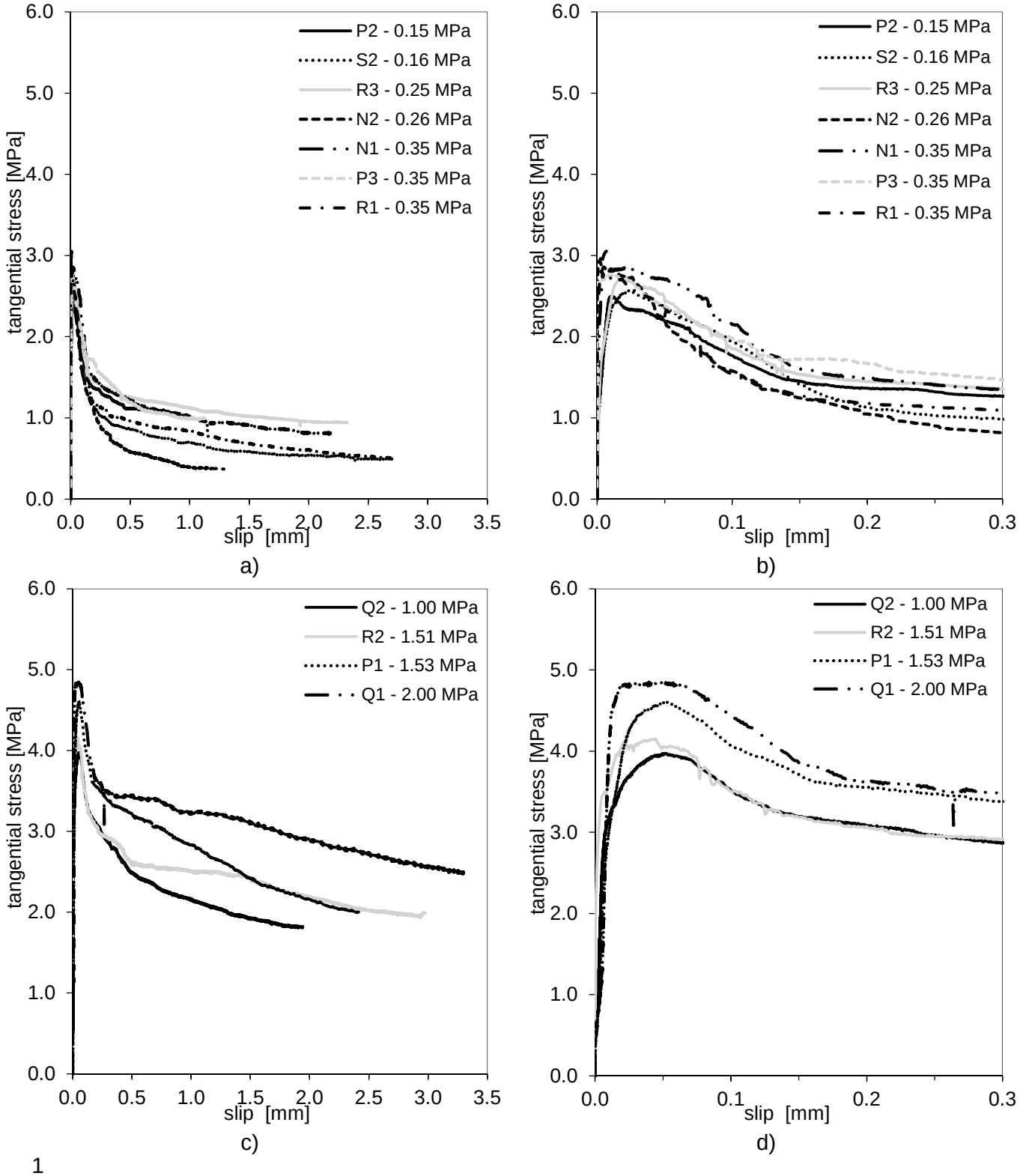

Figure 16 - τ-s responses for direction 2 (45º): a) and b) responses for lower imposed normal stresses; c) and d) responses for higher imposed normal stresses; b) and d) detail of the initial stage up to an average slip of 0.3mm.

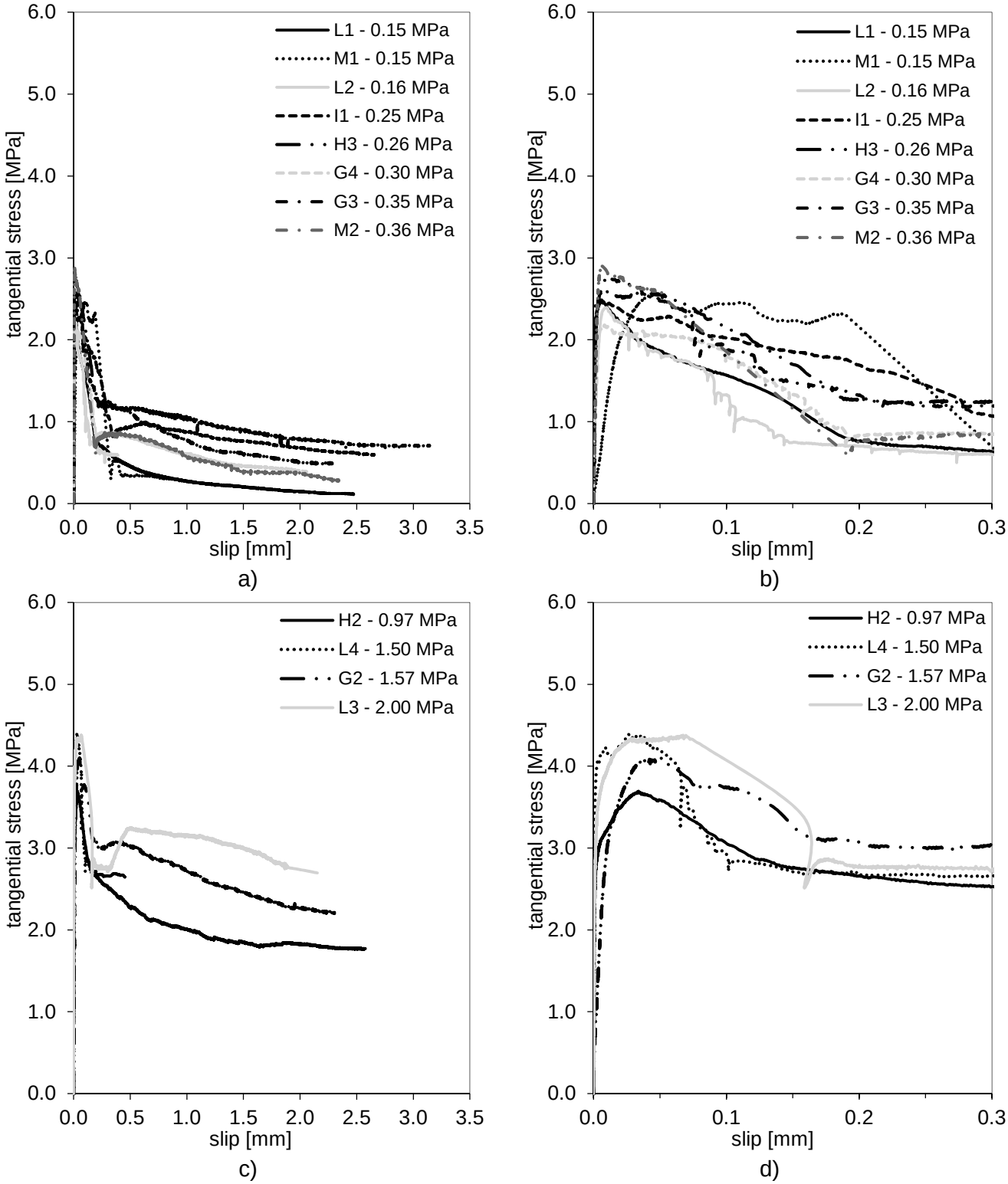

Figure 17 - τ-s responses for direction 3 (90º): a) and b) responses for lower imposed normal stresses; c) and d) responses for higher imposed normal stresses; b) and d) detail of the initial stage up to an average slip of 0.3mm.

4.3. Failure surfaces

For the specimens tested in direction 1 (0º) the failure was governed by the simple sliding of the opposite material surfaces respective to each other, whereas for the specimens tested in direction 3 (90º) the displacement perpendicular to the brick ribs led to the progressive failure of these ribs. For direction 2 (45º) the specimens showed a mixed type of failure. Figure 18 and Figure 19 present a few examples of representative failure surfaces obtained after testing.

Direction 1 (0º) Direction 2 (45º) Direction 3 (90º)

Figure 18 - Front view of the ruptured specimens after testing.

Direction 1 (0º) Direction 2 (45º) Direction 3 (90º)

Figure 19 - Opposite faces of the failure surfaces obtained after testing.

5. DISCUSSION OF RESULTS

5.1. Peak and residual shear stresses

Considering that the strengthening overlay in service conditions is typically subjected to low normal stresses, the characterization of the shear response of the interface was carried out initially considering normal stresses below 0.5 MPa. In Figure 20 to Figure 22, the results obtained for the shear strength versus the normal stress are analysed (negative values are considered for compression). Based on the assumption that the peak tangential stress increases linearly with the normal stress, the linear regression of the results was carried out. The estimation of the friction angle based on the slope of the linear regression has resulted in a value of 70º, 61º and 61º for directions 1, 2 and 3 respectively. These results are way beyond the values expected for the materials involved. As a result, it was decided to perform additional shear tests at higher values of the imposed normal stress, in order to better characterize the overall shape of the failure criterion. These additional tests were performed at normal stresses between -1 MPa and -2 MPa. Subsequently, the two different sets of data, i.e. for lower [-0.5 - 0] MPa and for higher [-2.0 - -1.0] MPa imposed normal stresses, were analysed separately, by performing individual linear regressions per each set. Identical analysis was performed for the residual shear stress values.

As shown in Figures Figure 20 to Figure 22 and in Table 5, the slope of the linear regressions obtained varies considerably for all three tested directions, depending on whether lower or higher imposed normal stresses are considered. Considering the peak tangential stresses, the slope obtained for higher imposed normal stresses is always significantly lower than the slope obtained for lower imposed normal stresses. As a result, both the hyperbolic Mohr and the linear Mohr-Coulomb criteria where adopted in order to replicate the experimentally obtained behaviours. In the case of the residual tangential stresses, the analysis considering only the results obtained for lower normal stresses can be misleading if analysed isolated. The coefficients of determination obtained by linear regression for directions 0º, 45º and 90º are low, especially in the case

of the 45º loading direction. As a consequence, the estimated values of the friction angle show some dispersion, especially in the case of the 45º loading direction. The analysis of results should therefore consider a wider range of results with both low and high confining stresses, preferably adopting a variable friction angle.

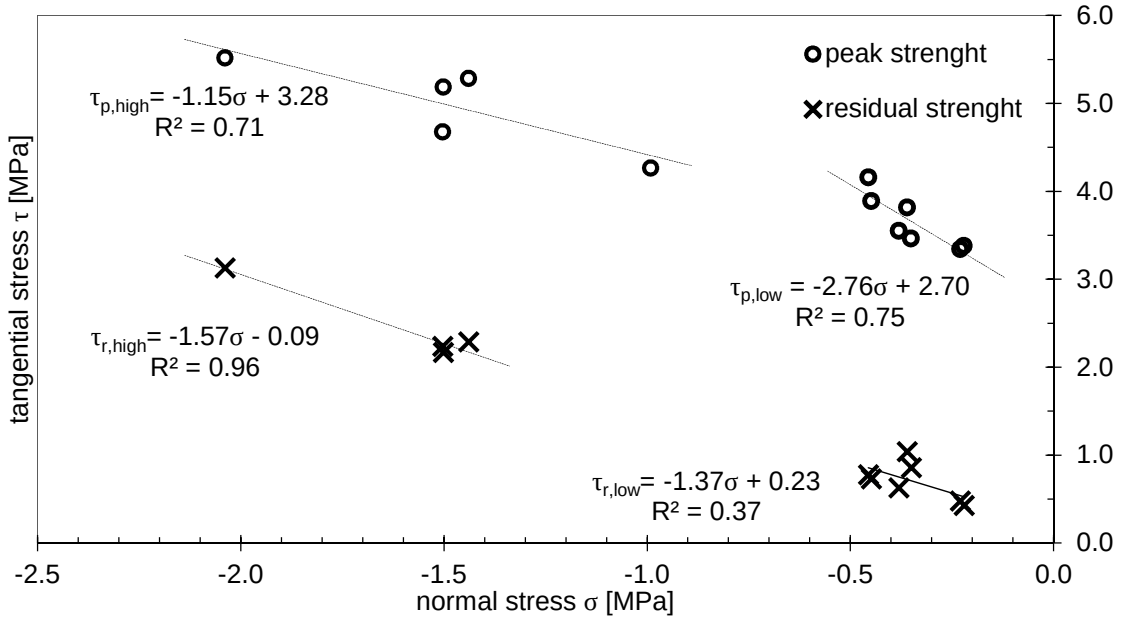

Figure 20 - Linear regressions for direction 1 (0º) considering peak and residual shear stress values.

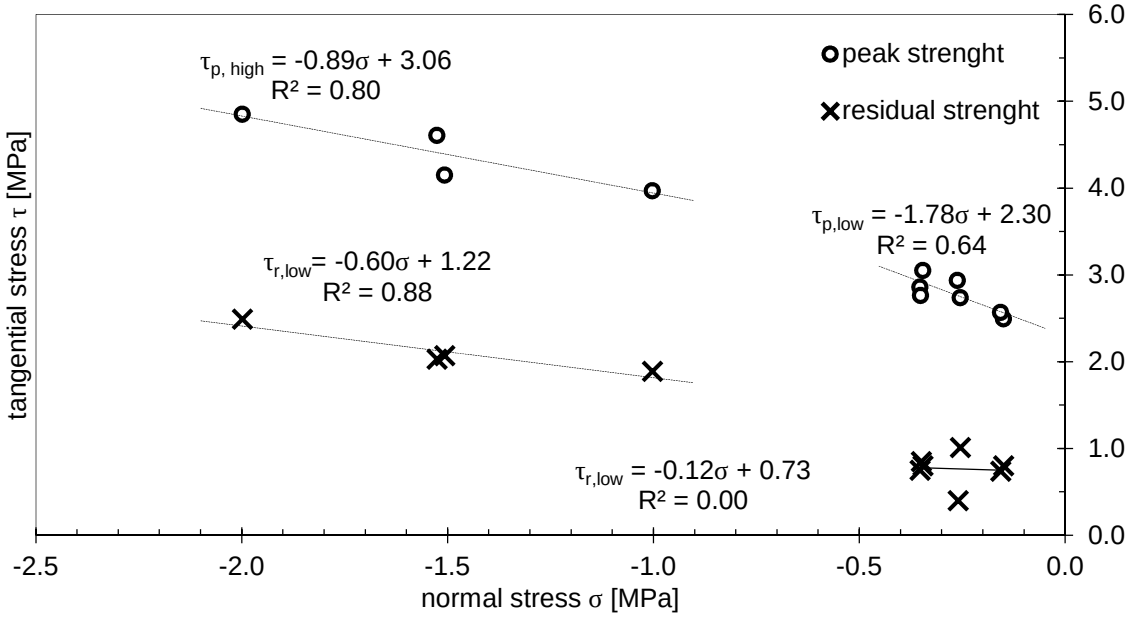

Figure 21 - Linear regressions for direction 2 (45º) considering peak and residual shear stress values.

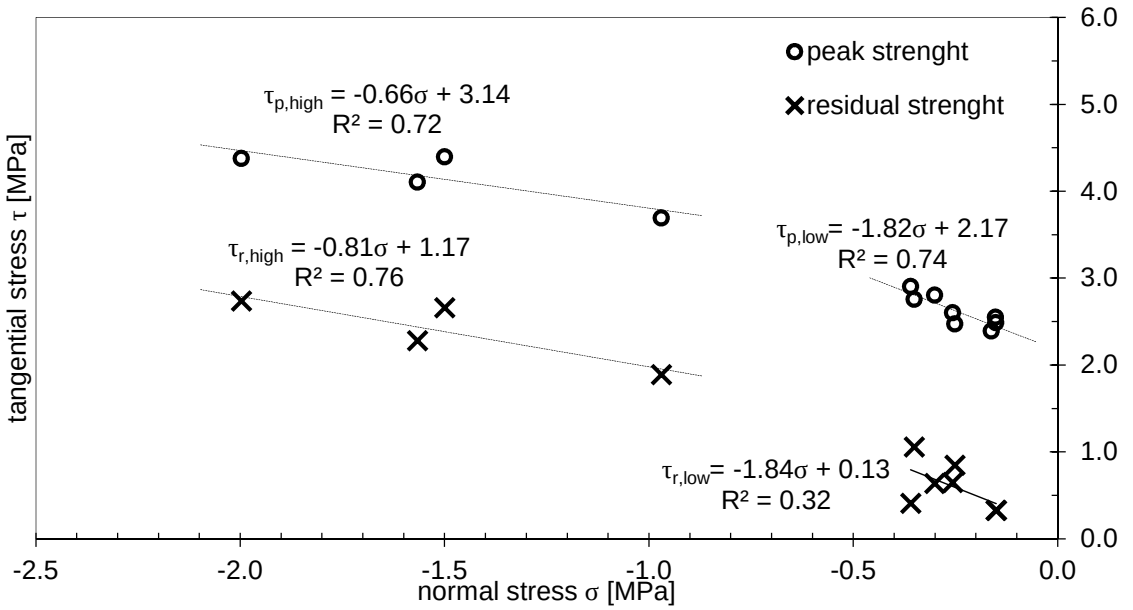

Figure 22 - Linear regressions for direction 3 (90º) considering peak and residual shear stress values.

Table 5 - Estimation of the friction angle for lower and higher normal stresses based on the linear regressions.

	Peak tangential stress		Residual tangential stress	
	Lower	Higher	Lower	Higher
Direction 1: 0º	70	49	54	58
Direction 2: 45º	61	42	7	31
Direction 3: 90º	61	33	61	39

5.2. Mohr Criterion

Considering the observed differences between the response parameters obtained for higher and lower normal stresses, the hyperbolic Mohr failure criterion was selected for modelling the interaction between the normal and the shear stress components in the entire range of imposed normal stresses tested. Due to its hyperbolic shape, this criterion is expected to describe well the results obtained for both the lower and the higher normal stresses studied. The mathematical equation used to describe the Mohr failure criterion in terms of the peak values of the shear stress is presented in equation (9):

$$\tau = \pm\sqrt{\left(c_p^* - \sigma \times \tan \emptyset_p\right)^2 - \left(c_p^* + \chi \times \tan \emptyset_p\right)^2} \qquad (9)$$

where τ is the tangential stress, σ is the normal stress, c_p^* is the apparent peak cohesion, $\emptyset_p$ is the peak friction angle and χ is the tensile strength.

The geometrical representation of the Mohr failure criterion is depicted in Figure 23, where the compressive normal stress is considered as negative in the horizontal axis.

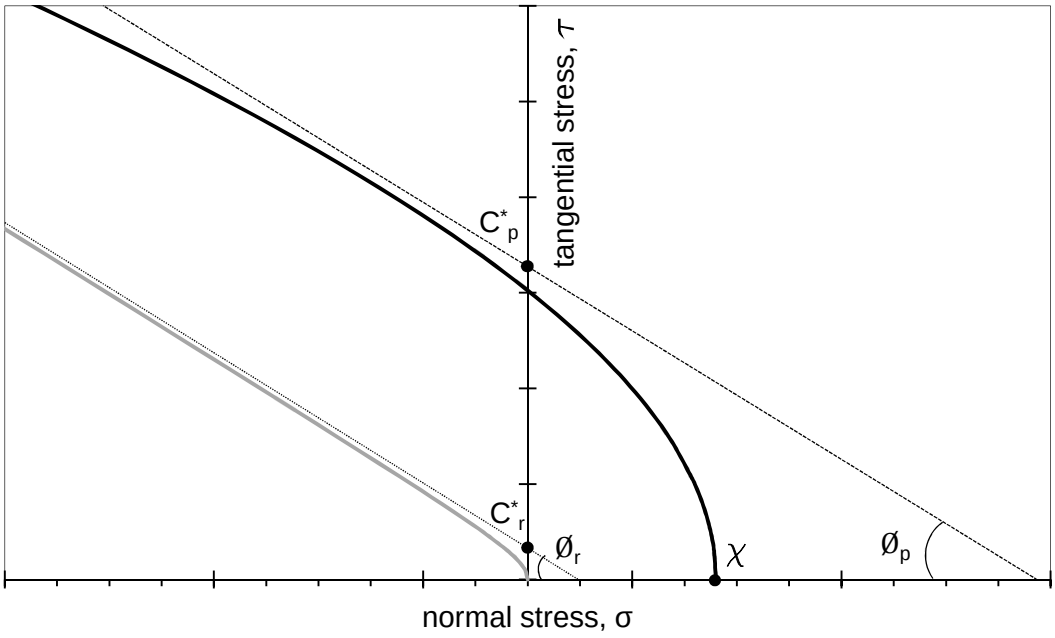

Figure 23 – Representation of the Mohr failure criterion when used to characterize the interaction between the normal stress and both the peak and residual values for positive tangential stresses. The subscript 'p' identifies the 'peak' failure surface parameters and the subscript 'r' identifies the 'residual' parameters.

The equation describing the Mohr failure criterion may also be used to describe the interaction between the normal stress and the residual shear stress, as shown in equation (11) and represented in Figure 23.

$$\tau = \pm\sqrt{(c_r^* - \sigma \times \tan \emptyset_r)^2 - (c_r^*)^2} \qquad (10)$$

where τ is the tangential stress, σ is the normal stress, c_r^* is the apparent residual cohesion and $\emptyset_r$ is the residual friction angle.

In this case the tensile strength parameter, χ, may be considered as zero due to the existence of a fully propagated crack along the interface, which implies the full separation of the two units forming the specimen if a tensile force is applied.

Regarding the peak results, the initial estimation of the friction angle, $\emptyset_{0,p}$, and initial apparent cohesion, $c_{0,p}^*$, was based on the previous linear regression analysis of the

experimental data. The value for $\emptyset_{0,p}$ was estimated based on the linear regression of the higher imposed normal stress values (see Figure 20 to Figure 22), while the value of $c_{0,p}^{*}$, was calibrated in order to satisfy, $\tau(\pm = 0) = c$, where c is the real cohesion estimated using the linear regression of the lower imposed normal stress results. The estimation of the tensile strength parameter, χ, was based on the pull-off test results solely, since it is not expected to be influenced by the loading direction with respect to the orientation of the brick ribs.

The correlation degree reached while approximating the experimental results with the values obtained from the hyperbolic Mohr failure criterion, was evaluated by the coefficient of determination, R^2, as shown in equation (11):

$$R^2 = 1 - \frac{\sum_{i-1}^{n}(\tau_i - \tau_{M\ hr,i})^2}{\sum_{i-1}^{n}(\tau_i - \bar{\tau})^2} \qquad (11)$$

Where n is the number of specimens, τ_i are the experimental data, $\bar{\tau}$ is the mean value of the experimental data, and $\tau_{M\ hr,i}$ are the expected values estimated by Equation (9) considering the parameters $\emptyset_p$, c_p^*, χ.

For each of the three loading orientations (0º, 45º and 90º) the initial parameters and the coefficients of determination obtained in each case are presented in Table 6.

Table 6 - Estimated peak parameters for each loading direction.

	Estimated parameters		
	0º	45º	90º
$c_{0,p}^{*}$ (MPa)	6.2	5.5	6.6
$\emptyset_{0,p}$ (º)	49	42	33
χ (MPa)	0.6	0.6	0.6
R^2	0.57	0.89	0.94

Subsequently, using a nonlinear optimization algorithm [37] for maximising the R^2, the parameters that better adjust the Mohr curve to the experimental results were obtained. The limits of the search space were set by imposing $c_p^* \leq c_{0,p}^*$ and $\emptyset_p \geq \emptyset_{0,p}$. Additionally, considering that the adhesion strengths obtained by means of pull-off tests typically underestimate the tensile strength at the interface, and based on previous results published in the literature [38], the parameter χ was increased by 50% and the value of 0.9 MPa was adopted. The results obtained are presented in Table 7.

Table 7 - Optimized peak values of Mohr criterion parameters for each loading direction.

	Optimized parameters		
	0º	45º	90º
c_p^* (MPa)	4.54	3.69	3.97
$\emptyset_p$ (º)	49.0	44.8	39.6
χ (MPa)	0.9	0.9	0.9
R^2	0.86	0.97	0.95

Regarding the residual results, the parameters c_r^* and $\emptyset_r$ were obtained by maximizing the coefficient of determination, R^2, with a nonlinear optimization algorithm. The values obtained for the parameters describing the Mohr criterion are presented in Table 8. The correlation degree is higher than 0.92 for all directions. Nevertheless, in the case of the 45º loading direction, the apparent residual cohesion and residual friction angle do not lie between the respective ones obtained for the 0º and 90º loading directions. If this consideration is imposed as a condition, the values of c_r^*=0.41 and $\emptyset_r$=52.4º are obtained for a coefficient of determination R^2 =0.82.

The results obtained for both peak and residual Mohr criteria for each loading direction are represented in Figure 24 to Figure 26, and compared with the experimental results.

Table 8 – Optimized residual values of Mohr criterion parameters for each loading direction.

	Direction		
	0º	45º	90º
c_r^* (MPa)	0.28	1.66	0.53
$\emptyset_r$ (º)	53.7	33.7	51.1
R^2	0.98	0.92	0.94

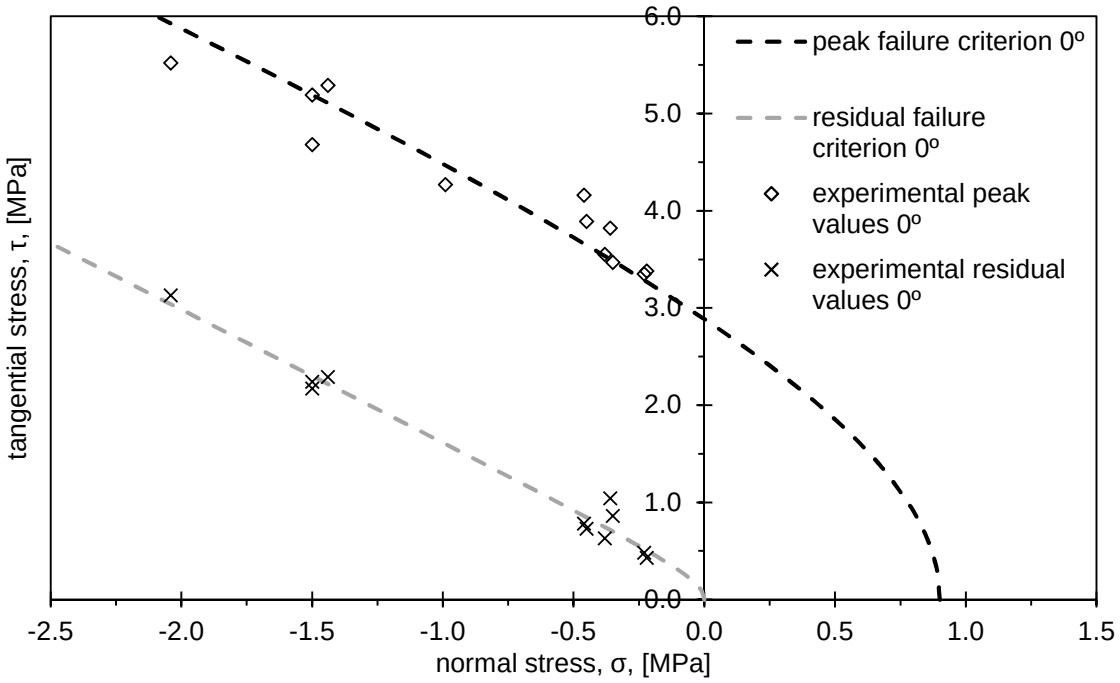

Figure 24 - Failure criteria for 0° loading direction.

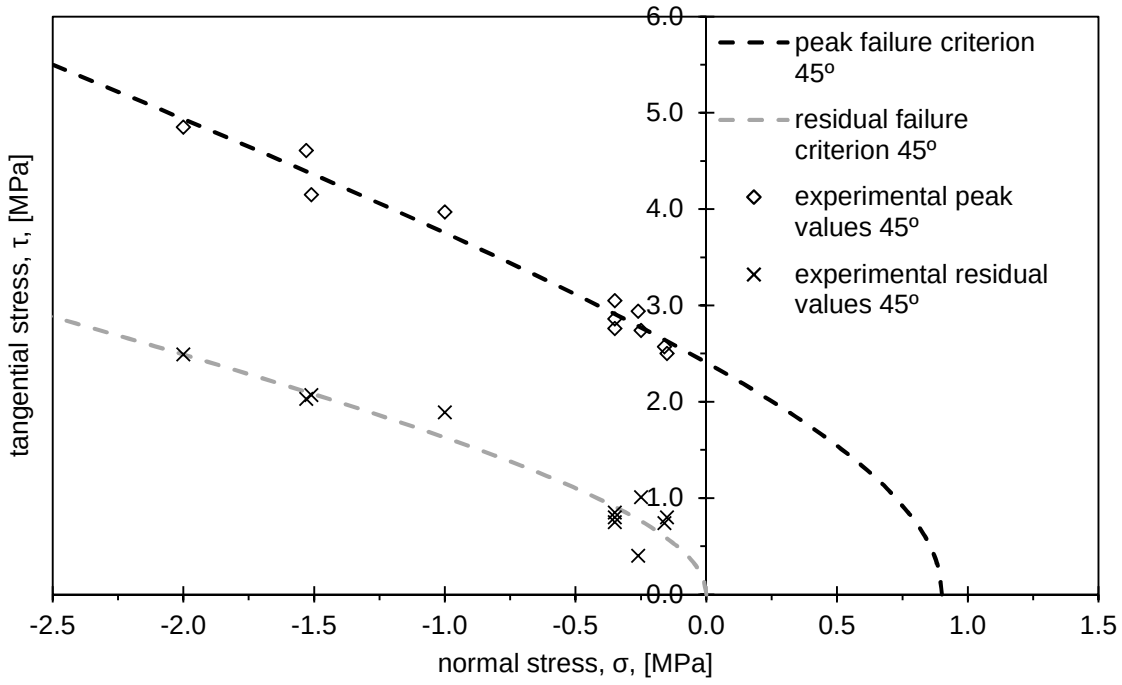

Figure 25 - Failure criteria for 45° loading direction.

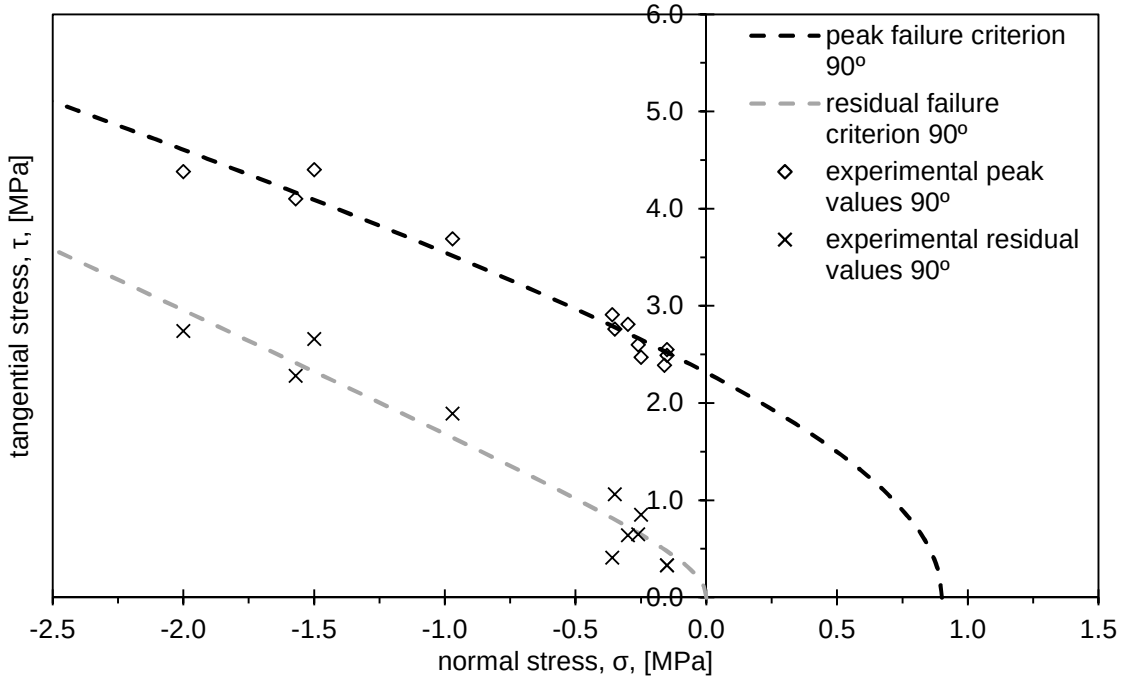

Figure 26 - Failure criteria for 90° loading direction.

5.3. Mohr-Coulomb criterion

The shape of the Mohr criterion proposed by Coulomb is simpler and consists of a line represented by the equation (3). This criterion may be used to describe the interaction between the normal stresses and both the peak and the residual shear stresses obtained

at the interface, as shown in Figure 27. Considering the peak shear stress results, the adjusted equation becomes:

$$f(\sigma) = c_p - \sigma \times \tan \emptyset_p \quad (12)$$

The parameters c_p and $\emptyset_p$ were evaluated by performing a linear regression of all the experimental results, as shown in Figure 28.

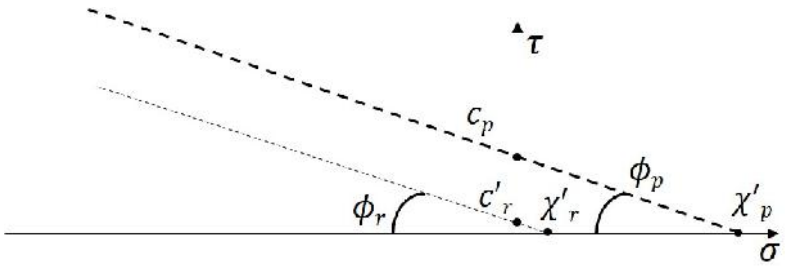

Figure 27 – Representation of the Mohr-Coulomb failure criteria for the peak and the residual shear stress results.

Considering the residual shear stress results, the formulation of the Mohr-Coulomb criterion must consider that the cohesion, c_r , should be approximately zero, as shown in Figure 27. Therefore the Mohr-Coloumb criterion is described by the equation (13):

$$\tau = c'_r - \sigma \times \tan \emptyset_r \quad (13)$$

where $\emptyset_r$ is the residual friction angle, and c'_r is the residual cohesion.

Considering the peak shear stress results, the linear regressions of the three sets of results obtained for the three loading directions show relatively high R^2 values, indicating that the linear approximation represents well the results obtained experimentally in the range of imposed normal stresses studied, see Figure 28. Nevertheless, the values obtained for χ', see Figure 27 and Table 9, are well above the tensile strengths obtained experimentally by means of the pull-off tests (0.57 MPa) or even the value adopted for the tensile strength, 0.9 MPa, that assures the maximum R^2 for the Mohr criterion (Table 7). The clear difference between these values indicates that the linear approximation is not appropriate to describe the interface behaviour outside the range of the data experimentally observed, in particular in the tensile normal stresses quadrant.

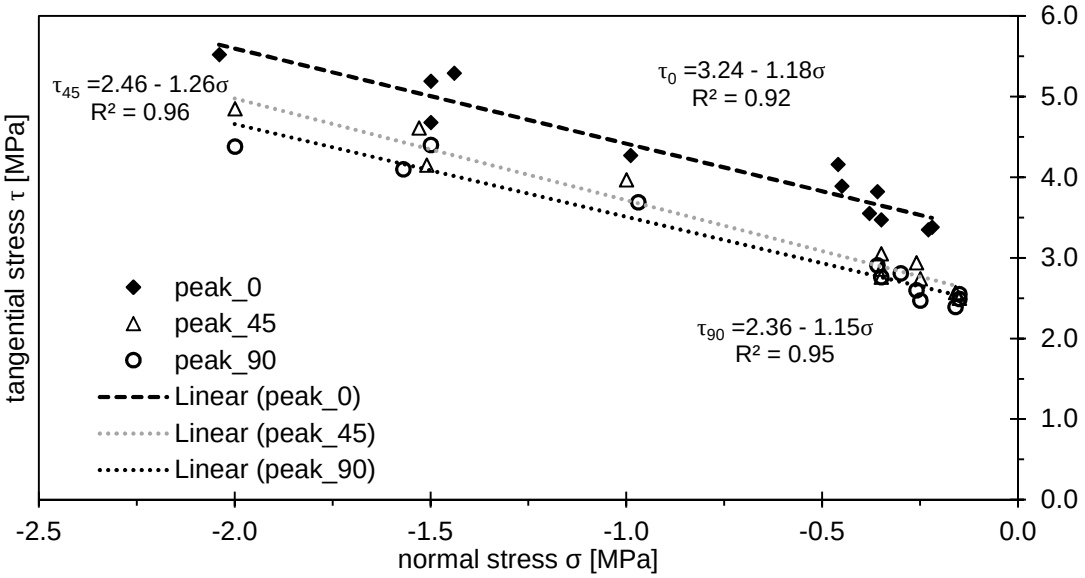

Figure 28 – Linear regression of the peak shear stress results for all orientations.

Table 9 - Estimated parameters considering the Mohr-Coulomb criterion and the peak shear stress results.

Direction	c_p (MPa)	$\emptyset_p$ (°)	R^2 --	χ' (MPa)
1 (0°)	3.24	50	0.92	2.74
2 (45°)	2.46	52	0.96	1.95
3 (90°)	2.36	49	0.95	2.05

Figure 29 shows that the obtained residual shear stress results are in general quite similar, with a slight distinction in the case of the 45º orientation with respect to the loading direction. Nevertheless, the R^2 values are significantly high for all loading directions. The linear regression of the experimental results led to residual values for cohesion, c_r, between 0.22 and 0.52 MPa, although the expected result would be zero. In the case of the residual tensile strength, χ', the results obtained vary between 0.16 and 0.50, see Table 10, which correspond to residual friction angles, $\emptyset_r$, varying between 46º and 54º.

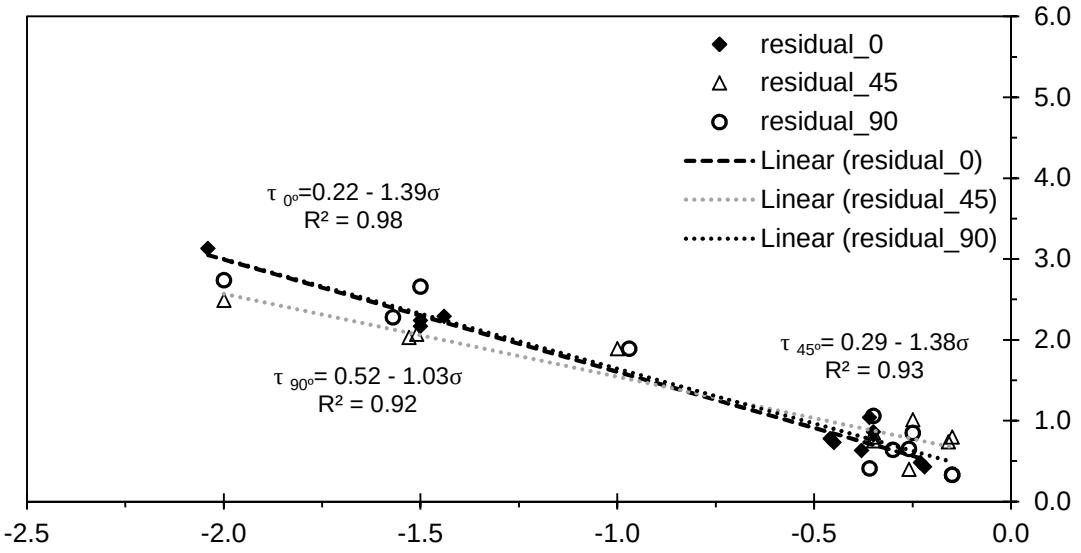

Figure 29 - Linear regression of the residual shear stress results for all orientations.

Table 10 - Estimated parameters considering the Mohr-Coulomb criterion for the residual shear stress results.

Direction	$\emptyset_r$ (°)	R^2 --	c_r'	χ' MPa
1 (0°)	54	0.98	0.22	0.16
2 (45°)	54	0.93	0.29	0.21
3 (90°)	46	0.92	0.52	0.50

5.4. Suitability of the criteria for describing the interface shear response

5.4.1. Comparison of Mohr and Mohr-Coulomb criteria

In order to compare the suitability of the Mohr-Coulomb linear criterion and the Mohr non-linear criterion for describing the experimental results, the experimental values of the shear stress, τ_e , were compared with the estimated ones, $y(\tau_e) = \tau_c$. The two previously mentioned criteria were adopted to estimate the peak and the residual tangential stresses obtained in the experimental responses for the different levels of imposed normal stresses. The values used to compare the criteria are presented in Table 7 and Table 8 for the Mohr criterion, in the case of the Mohr-Coulomb criterion the values are presented in Table 9 and Table 10.

The fitting quality of the criteria was assessed by computing the R^2 coefficient presented in equation (14):

$$R^2 = 1 - \frac{\sum_{i=1}^{n}(\tau_{c,i} - \tau_{e,i})^2}{\sum_{i=1}^{n}(\tau_{e,i} - \bar{\tau}_{e})^2} \quad (14)$$

where $\tau_{c,i}$ are the values estimated by the criteria and $\tau_{e,i}$ and $\bar{\tau}_{e}$ are, respectively, the experimental values and the mean value of the experimental results.

The results estimated using the expressions of Mohr and Mohr-Coulomb criteria are compared with the corresponding experimental results in Figure 30 to Figure 32. The fitting quality of the criteria was assessed by computing the R^2 values, as presented in Table 11. As shown, for all three loading directions the non-linear Mohr criterion presents a better fitting to the residual experimental results. The Mohr-Coulomb criterion adjusts better to the peak experimental results. Nonetheless it is worth to mention that both criteria present a good fitting to the experimental results.

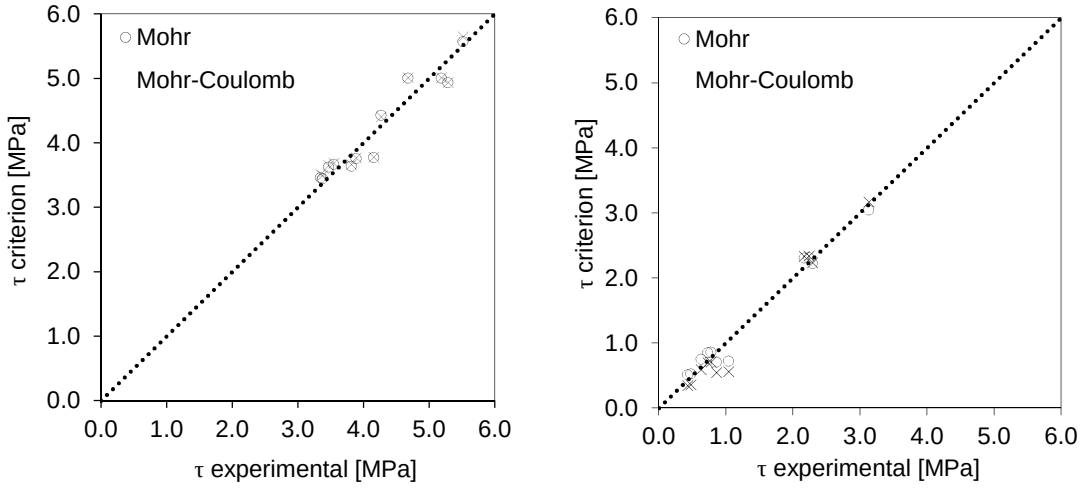

Figure 30 - Experimental versus criterion estimations for 0º loading direction: a) peak shear stresses; b) residual stresses.

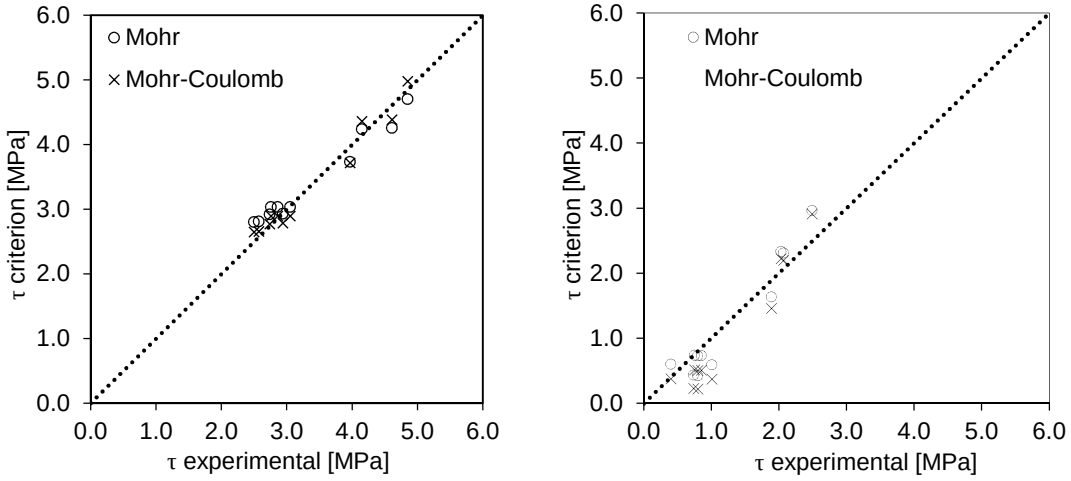

a) b)

Figure 31 – Experimental versus criterion estimation for 45º loading direction: a) peak shear stresses; b) residual shear stresses.

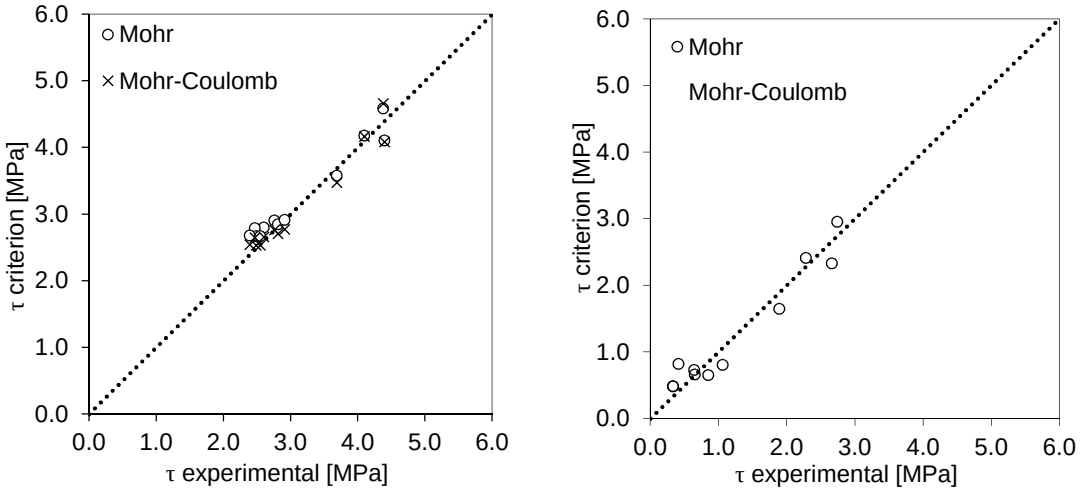

a) b)

Figure 32 - Experimental versus criterion estimations for 90º loading direction: a) peak shear stresses; b) residual shear stresses.

Table 11 - Summary of the R^2 values obtained for each testing direction.

	Peak criteria		Residual criteria	
Direction	Mohr R^2	Mohr-Coulomb R^2	Mohr R^2	Mohr-Coulomb R^2
1 (0°)	0.90	0.97	0.98	0.98
2 (45°)	0.97	0.96	0.92	0.89
3 (90°)	0.96	0.95	0.94	0.80

5.4.2. Criterion for the interface behaviour

As discussed, the failure behaviour observed in all experiments was appropriately described by the two criteria. In general, both criteria present good correlation with the experimental results, although the Mohr criterion can better describe the behaviour of the interface also in the tensile region, as shown Figure 32. Nonetheless, it became evident that the possibility to further characterize the interface shear stress-slip response in the tensile region would be beneficial for defining the optimal parameters in each case. However the test setup would have to be adapted in order to allow combining shear and tensile loads during testing.

The failure criterion for peak shear stresses in the case of the loading direction 2 (45° orientation) assumed approximately an intermediate behaviour between the criteria deduced for 0° and 90° loading directions. In the case of the residual criterion this effect was not so clear, as shown in Figure 33. The surface obtained by combining the failure criteria for all directions is represented in Figure 34. The values for loading directions different from 0º, 45º and 90º were estimated based on a linear interpolation between the known values of the 0º, 45º and 90º curves.

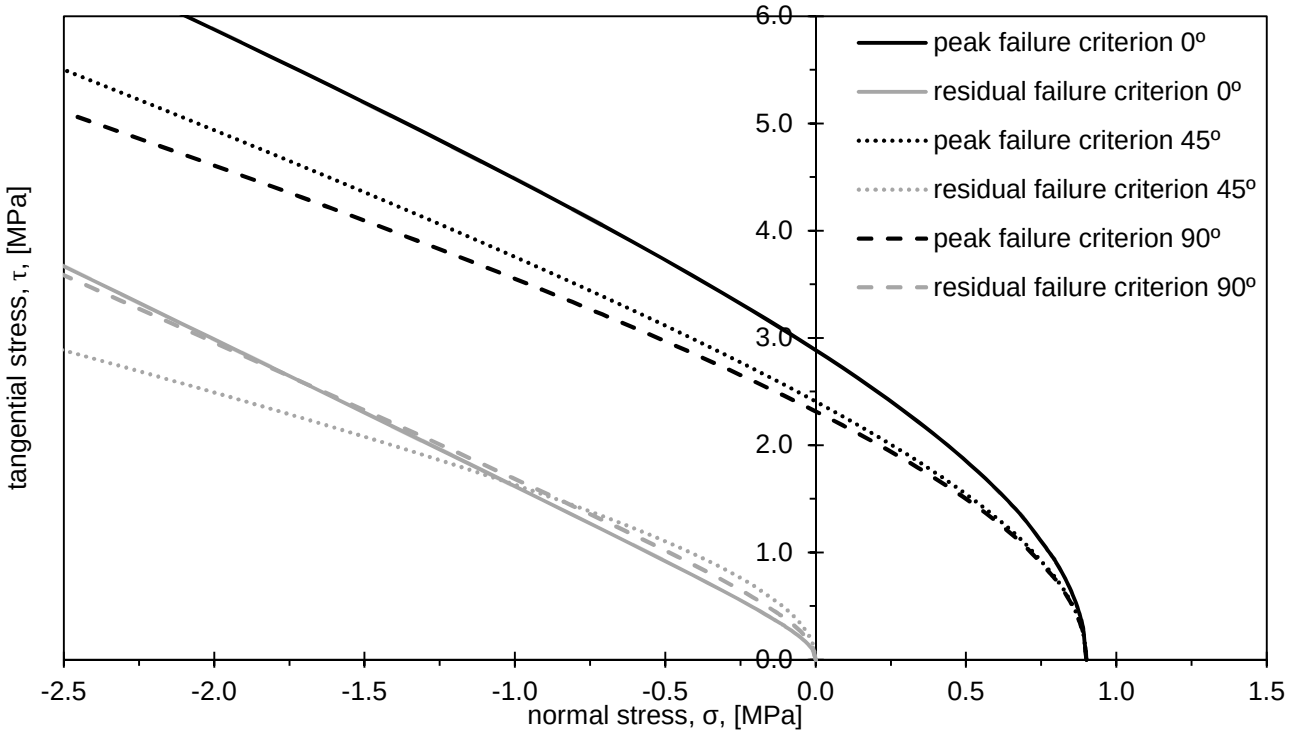

Figure 33 – Failure criteria for peak and residual shear stress.

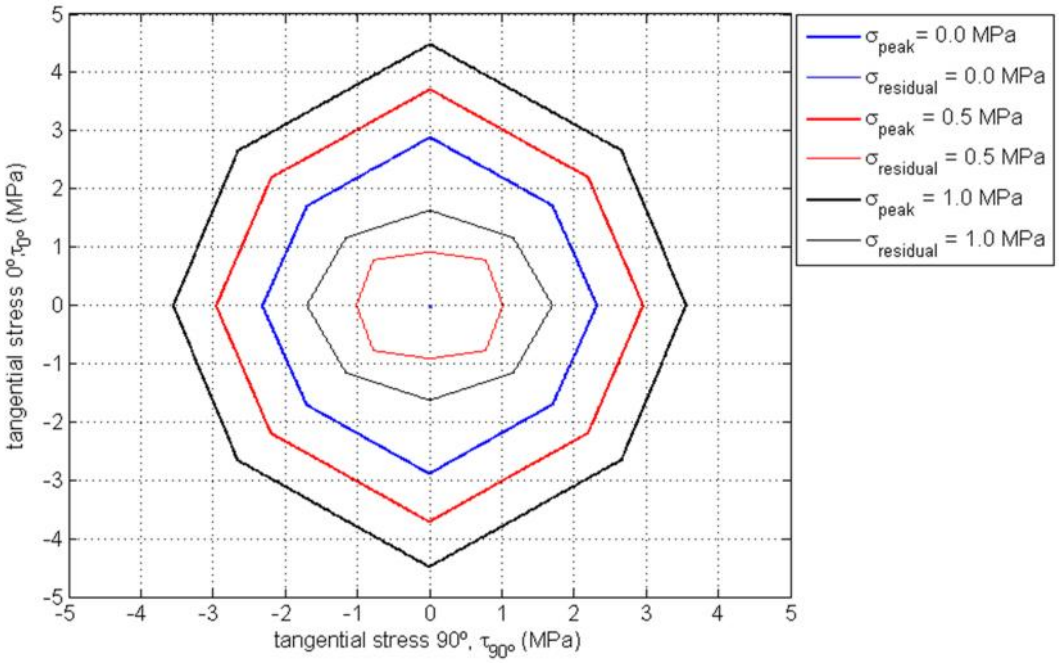

a)

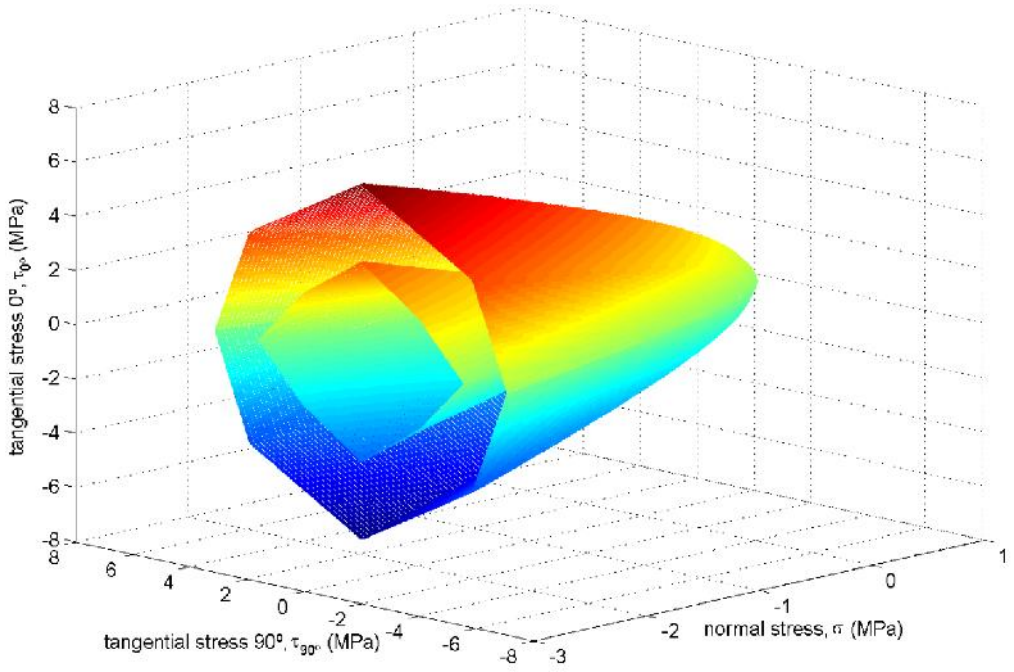

b)

Figure 34 – Combined failure criteria for all directions: a) representation of the peak and residual values for 0, 0.5 and 1.0 MPa normal stresses; b) 3D orthotropic representation of the peak and residual loading/failure criteria.

6. CONCLUSIONS

The test setup developed in this research aimed to assure a direct characterization of the interface behaviour between a ceramic brick substrate and the PFRM strengthening overlay. The results obtained showed the consistent development of a single failure surface for all specimens throughout the entire testing program, which is important for the objective characterization of the mechanical response of the interface. This feature is beneficial when compared with other test setups used in the characterization of the interface between two materials, for instance because there is no interaction between multiple failure surfaces or interfaces, which generally occurs when triplet test is used.

The brick surface type used was characterized by a principal direction of the surface ribs. A global overview on the anisotropic interface behaviour was obtained by applying the shear force along three different loading directions (*0°, 45°, 90°*).

The experimental results showed in general a brittle post-peak behaviour and the achievement of a frictional residual strength related with the loading direction. When the

shear load was parallel to the brick ribs (0°), the failure surface was formed along the ribs together with the detachment of the two different materials and with negligible failure of the ribs on the brick surface and on the PFRM unit. A completely different failure characterized the 90° orientation series. The displacement imposed perpendicularly to the ribs caused a progressive cracking of the ribs on the brick surface. The intermediate orientation displayed a mixed behaviour.

The most suitable failure criterion to predict the experimental results is the hyperbolic approximation from the Mohr criterion, this criterion can predict the values in a wider range of data, including lower values of normal stress. For all tested directions, the correlation degree reached while approximating the experimental results, evaluated by the coefficient R^2, was higher than 0.90 for the peak shear stress and higher than 0.92 for the residual shear stress. In addition, it was found that the range of normal stresses considered to deduce the parameters of the loading/failure criterion had a significant impact on the results obtained. In particular, the value of the friction angle was very sensitive to the range of normal stresses considered to derive the Mohr-Coloumb loading/failure criterion parameters.

The testing procedure studied in this research could be further used to characterize the shear response for other loading orientations with respect to the brick ribs in order to have a complete overview on the orthotropic interface behaviour. Direct shear cyclic tests could also be performed in order to assess the influence of load inversion on the behaviour of the interface between the substrate and the reinforcing layer. These results can in the future be used to extend the interface constitutive criteria for simulating cyclic loading conditions.

Acknowledgements

This research was carried in the framework of InoTec, Innovative material of ultra-high ductility for the rehabilitation of the built patrimony, funded by COMPETE/QREN/FEDER

(NORTE-07-0202-FEDER-023024). InoTec project is promoted by CiviTest company and University of Minho. S&P Clever Reinforcement Ibérica is gratefully acknowledged for providing the materials used in the strengthening of the masonry specimens.

References

[1] J. A. P. P. Almeida, E. B. Pereira, and J. A. O. Barros, “Assessment of overlay masonry strengthening system under in-plane monotonic and cyclic loading using the diagonal tensile test,” *Constr. Build. Mater.*, vol. 94, pp. 851–865, Sep. 2015.

[2] M. A. Elgawady, P. Lestuzzi, and M. Badoux, “A review of conventional seismic retrofitting techniques for URM,” in *13th International Brick and Block Masonry Conference*, 2004, pp. 1–10.

[3] H. Shakib, M. Mousavi, M. K. H. Rezaei, S. Dardaei, M. Ahmadizadeh, and M. Samadian, “Analytical and Experimental Seismic Evaluation of Unreinforced Masonry Walls Retrofitted by Shotcrete and CFRP Strips,” in *12th Canadian Masonry Symposium*, 2013, pp. 1–10.

[4] S. B. Kadam, Y. Singh, and B. Li, “Strengthening of unreinforced masonry using welded wire mesh and micro-concrete – Behaviour under in-plane action,” *Constr. Build. Mater.*, vol. 54, pp. 247–257, 2014.

[5] A. Figueiredo, H. Varum, A. Costa, D. Silveira, and C. Oliveira, “Seismic retrofitting solution of an adobe masonry wall,” *Mater. Struct.*, vol. 46, no. 1–2, pp. 203–219, Jul. 2012.

[6] C. G. Papanicolaou, T. C. Triantafillou, K. Karlos, and M. Papathanasiou, “Textile-reinforced mortar (TRM) versus FRP as strengthening material of URM walls : in-plane cyclic loading,” *Mater. Struct.*, vol. 40, pp. 1081–1097, 2007.

[7] E. Bernat-Maso, C. Escrig, C. A. Aranha, and L. Gil, “Experimental assessment of Textile Reinforced Sprayed Mortar strengthening system for brickwork wallettes,” *Constr. Build. Mater.*, vol. 50, pp. 226–236, 2014.

[8] M. Corradi, A. Borri, G. Castori, and R. Sisti, “Shear strengthening of wall panels through jacketing with cement mortar reinforced by GFRP grids,” *Compos. Part B Eng.*, vol. 64, pp. 33–42, 2014.

[9] Federal Emergency Management Agency, *Techniques for the Seismic Rehabilitation of Existing Buildings - FEMA 547*. Books Express Publishing, 2006, p. 572.

[10] Y. Kim, H. Kong, and V. C. Li, “Design of engineered cementitious composite suitable for wet-mixture shotcreting,” *ACI Mater. J.*, no. 100, 2003.

[11] E. Esmaeeli, E. Manning, and J. A. O. Barros, “Strain hardening fibre reinforced cement composites for the flexural strengthening of masonry elements of ancient structures,” *Constr. Build. Mater.*, vol. 38, pp. 1010–1021, Jan. 2013.

[12] A. Dehghani, G. Fischer, and F. Alahi, “Strengthening masonry infill panels using engineered cementitious composites,” *Mater. Struct.*, 2013.

[13] M. A. Elgawady, P. Lestuzzi, and M. Badoux, “Retrofitting of masonry walls using shotcrete,” in *NZSEE Conference, Yeni Zelanda*, 2006, no. 45.

[14] M. R. Valluzzi, D. Tinazzi, and C. Modena, “Shear behavior of masonry panels strengthened by FRP laminates,” *Constr. Build. Mater.*, vol. 16, no. 7, pp. 409–416, Oct. 2002.

[15] S. S. Prakash and P. Alagusundaramoorthy, “Load resistance of masonry wallettes and shear triplets retrofitted with GFRP composites,” *Cem. Concr. Compos.*, vol. 30, no. 8, pp. 745–761, Sep. 2008.

[16] A. Bruedern, D. Abecasis, and V. Mechtcherine, “Development of Strain-Hardening Cement-based Composites for the strengthening of masonry,” in *Concrete Repair, Rehabilitation and Retrofitting II - Proceedings of the 2nd International Conference on Concrete Repair, Rehabilitation and Retrofitting, ICCRRR*, 2009, pp. 887–894.

[17] B. V. Venkatarama Reddy and C. V. Uday Vyas, “Influence of shear bond strength on compressive strength and stress–strain characteristics of masonry,” *Mater. Struct.*, vol. 41, no. 10, pp. 1697–1712, Jan. 2008.

[18] G. F. M. Vasconcelos and P. B. Lourenço, “Experimental characterization of stone masonry in shear and compression,” *Constr. Build. Mater.*, vol. 23, no. 11, pp. 3337–3345, Nov. 2009.

[19] V. Alecci, M. Fagone, T. Rotunno, and M. De Stefano, “Shear strength of brick masonry walls assembled with different types of mortar,” *Constr. Build. Mater.*, vol. 40, pp. 1038–1045, Mar. 2013.

[20] L. Abdou, R. A. Saada, F. Meftah, and A. Mebarki, “Experimental investigations of the joint-mortar behaviour,” *Mech. Res. Commun.*, vol. 33, pp. 370–384, 2006.

[21] N. Augenti and F. Parisi, “Constitutive modelling of tuff masonry in direct shear,” *Constr. Build. Mater.*, vol. 25, no. 4, pp. 1612–1620, 2011.

[22] R. van der Pluijm, *Out-of-Plane Bending of Masonry Behaviour and Strength*. R. van der Pluijm, 1999, p. 259.

[23] M. Montazerolghaem and W. Jaeger, “A Comparative Numerical Evaluation of Masonry Initial Shear Test Methods and Modifications Proposed for EN 1052-3,” in *9th International Masonry Conference, July 7, 8, 9; 2014; Guimarães*, 2014, pp. 1–10.

[24] Comité Européen de Normalisation, “EN 1052-3:2002 Methods of test for mortar masonry - Part 3: Determination of inicial shear strength,” vol. 3, no. c. Comité Européen de Normalisation, Brussels, p. 14, 2002.

[25] J. Hofmann, P.; Stöckl, S.; Mainz, “A comparative finite element evaluation of mortar joint shear tests,” *Mason. Int.*, vol. 3, no. 3, pp. 101–104, 1990.

[26] P. B. Lourenço, J. A. O. Barros, and J. T. Oliveira, “Shear testing of stack bonded masonry,” *Constr. Build. Mater.*, vol. 18, no. 2, pp. 125–132, Mar. 2004.

[27] A. Gabor, A. Bennani, E. Jacquelin, and F. Lebon, “Modelling approaches of the in-plane shear behaviour of unreinforced and FRP strengthened masonry panels,” *Compos. Struct.*, vol. 74, pp. 277–288, 2006.

[28] J. Milosevic, A. S. Gago, M. Lopes, and R. Bento, “Experimental assessment of shear strength parameters on rubble stone masonry specimens,” *Constr. Build. Mater.*, vol. 47, pp. 1372–1380, Oct. 2013.

[29] W.-F. Chen, *Plasticity in reinforced concrete*. J. Ross Publishing, 2007, p. 474.

[30] I. Carol and P. C. Prat, “Normal/shear cracking model: Application to discrete crack analysis,” *J. Eng. Mech.*, vol. 123, no. 8, p. 765, Aug. 1997.

[31] J. Heyman, *Coulomb’s Memoir on Statics: An Essay in the History of Civil Engineering*. London: Imperial College Press, 1997.

[32] A. Caggiano, G. Etse, and E. Martinelli, “Zero-thickness interface model formulation for failure behavior of fiber-reinforced cementitious composites.,” *Comput. Struct.*, vol. 98–99, pp. 23–32, May 2012.

[33] C. M. López, I. Carol, and A. Aguado, “Meso-structural study of concrete fracture using interface elements . I : numerical model and tensile behavior,” *Mater. Struct.*, no. 41, pp. 583–599, 2008.

[34] Comité Européen de Normalisation, “EN 772-1:2000 Methods of test for masonry units. Determination of compressive strength.” Comité Européen de Normalisation, Brussels, p. 14, 2000.

[35] Comité Européen de Normalisation, “EN 1015-11:1999 Methods of test mortar for masonry – Part 11: Determination of flexural and compressive strength of hardened mortar.” Brussels, 1999.

[36] Comité Européen de Normalisation, “EN 1015-12:2000 Methods of test for mortar for masonry - Part 12: Determination of adhesive strength of hardened mortar.” Brussels, 2000.

[37] I. Nenov and D. Fylstra, “Interval Methods for Accelerated Global Search in the Microsoft Excel Solver,” *Reliab. Comput.*, vol. 9, no. 2, pp. 143–159, 2003.

[38] L. Courard, B. Bissonnette, A. Garbacz, A. Vaysburd, K. Von Fay, G. Moczulski, and M. Morency, “Effect of Misalignment on Pull-off Test Results : Numerical and Experimental Assessments,” *ACI Mater. J.*, no. 111, pp. 153–162, 2014.